Collision of vortex-rings upon V-walls

T. H. New[1]†, J. Long[1], B. Zang[1,2] and Shengxian Shi[3]

[1]School of Mechanical and Aerospace Engineering, Nanyang Technological University
50 Nanyang Avenue, Singapore 639798

[2]Presently at Department of Aerospace Engineering, University of Bristol
United Kingdom, BS8 1TR

[3]School of Mechanical Engineering, Shanghai Jiao Tong University
800 Dong Chuan Road, Shanghai, China 200240

(Received xx; revised xx; accepted xx)

A study on Re=2000 and 4000 vortex-rings colliding with V-walls with included-angles of θ=30° to 120° had been conducted. Along the valley-plane, higher Reynolds numbers and/or included-angles of $\theta \leqslant 60°$ lead to secondary/tertiary vortex-ring cores leapfrogging past the primary vortex-ring cores. The boundary layers upstream of the latter separate and the secondary/tertiary vortex-ring cores pair up with these wall-separated vortices to form small daisy-chained vortex-dipoles. Along the orthogonal-plane, primary vortex-ring cores grow bulbous and incoherent after collisions, especially as the included-angle reduces. Secondary and tertiary vortex-ring core formations along this plane also lag those along the valley-plane, indicating they form by propagating from the wall surfaces to the orthogonal-plane as the primary vortex-ring gradually comes into contact with the entire V-wall. Circulation results show significant variations between the valley- and orthogonal-plane and reinforce the notion that the collision behaviour for $\theta \leqslant 60°$ is distinctively different from those at larger included-angles. Vortex-core trajectories are compared to those for inclined-wall collisions and secondary vortex-ring cores are found to initiate earlier for the V-walls, postulated to be a result of the opposing circumferential flows caused by the simultaneous collisions of both primary vortex-ring cores with the V-wall surfaces. These circumferential flows produce a bi-helical flow mode [Lim (1989)] that sees higher vortex compression levels along the orthogonal-plane, which limit vortex-stretching along the wall surfaces and produce secondary vortex-rings earlier. Lastly, vortex structures and behaviour of the present collisions are compared to those associated with flat/inclined-walls and round cylinder based collisions for a more systematic understanding of their differences.

Key words:

1. Introduction

Vortex-rings have always fascinated fluid dynamists at large, due to their structural simplicity and relevance towards much more complex flow scenarios that in turn lend themselves towards engineering flow applications such as synthetic jets for flow control purposes [Amitay *et al.* (2001); Gilarranz *et al.* (2005); You & Moin (2008)], impinging jets for heat transfer applications [Martin (1977); Goldstein & Franchett (1988); Hadžiabdić & Hanjalić (2008); New & Long (2015)], vortex-ring state in helicopter flights

† Email address for correspondence: dthnew@ntu.edu.sg

[Newman *et al.* (2001); Leishman *et al.* (2004); Johnson (2005)], and more recently, particle-shaping techniques [An *et al.* (2016); Zhan *et al.* (2017)], among others. It should come as no surprise then that significant research has been expended to expand our fundamental understanding of vortex-rings and how they interact with their surroundings. Take for instance, more recent studies on the behaviour of translating discrete circular vortex-rings would include Maxworthy (1972), Didden (1979), Pullin (1979), Glezer (1988), Glezer & Coles (1990), Nitsche & Krasny (1994), R. S. Heeg & Riley (1997), Gharib *et al.* (1998), Mohseni & Gharib (1998), Mohseni *et al.* (2001), Krueger *et al.* (2003), Krueger *et al.* (2006), Shusser *et al.* (2006), Kaplanski *et al.* (2009), Feng *et al.* (2009), Gao & Yu (2010), Gan *et al.* (2012), Ponitz *et al.* (2016) and Mao & Hussain (2017), among many others. These investigations primarily focused upon how initial and boundary conditions affect vortex-ring generation, nature of laminar and turbulent vortex-ring formations and propagations, vortex-ring formation time-scales, azimuthal wave instabilities, relationships between the initial vortex-rings in starting-jets and other important characteristics.

Many experimental and numerical studies had also been conducted for vortex-ring collision scenarios. Such scenarios will be of special interest, as it entails the direct impact and subsequent interactions between two vortex-rings or a vortex-ring and solid/non-solid boundaries, as opposed to a discrete vortex-ring entity assumed to be or largely free of external influences. Such scenarios had been studied systematically earlier, including but not limited to those reported by Walker *et al.* (1987), Lim (1989), Lim *et al.* (1991), Orlandi & Verzicco (1993), Verzicco & Orlandi (1994), Chu *et al.* (1995), Swearingen *et al.* (1995), Fabris *et al.* (1996), Minota *et al.* (1997), Naitoh *et al.* (2001), Arévalo *et al.* (2007), Cheng *et al.* (2010), Couch & Krueger (2011), Mariani *et al.* (2013), Xu & Wang (2016) and New *et al.* (2016) for flat/inclined-walls; Adhikari & Lim (2009), Naaktgeboren *et al.* (2012), Hrynuk *et al.* (2012), Cheng *et al.* (2014) and Xu *et al.* (2018) for porous walls; Orlandi (1993), Naitoh *et al.* (1995), Ren *et al.* (2015) and New & Zang (2017) for round cylinders; and more recently, Hu & Peterson (2018) investigated a scenario whereby a vortex-ring collides upon a wall with a circular aperture.

Recently, New *et al.* (2018) conducted a limited study to explore Re=1000 vortex-rings impacting upon V-walls, a configuration of which can essentially be treated as two single inclined-walls arranged and joined at the apex symmetrically. While many vortex-ring collisions had been based on flat/inclined-walls, V-wall configurations have not been systematically explored before. There are several interesting key differences between the use of V-walls and other wall types for vortex-ring collisions that ought to be highlighted. Firstly, when compared to an inclined-wall, a V-wall poses a far more physically constrained boundary condition where the vortex-ring motion will be physically limited by the valley downstream of the collision axis. As such, more extensive vortical motions along the orthogonal-plane of the V-wall will be expected. Secondly, two vortex-ring segments will collide with both V-wall surfaces simultaneously and symmetrically, as opposed to one colliding after another for an inclined-wall. As such, the overall three-dimensional flow dynamics are expected to deviate from but continue to be inspired by the bi-helical line flow model first put forward by Lim (1989) and confirmed by Verzicco & Orlandi (1994) and New *et al.* (2016) for inclined-wall collisions. Furthermore, in contrast to vortex-ring collisions upon more convex surfaces such as round cylinders, V-wall collisions will provide some key insights into the resulting flow structures and behaviour when more concave-like wall types are used instead, even if curvature effects are not accounted for.

The present study follows up and expands upon the earlier study by experimentally investigating Re=2000 and 4000 vortex-ring collisions upon V-walls with included-angles

ranging from 30° to 120° at 30° intervals. In particular, the use of additional higher Reynolds numbers and V-walls here are expected to shed more light upon the effects of various parameters. The present objectives are to provide more definitive information along several research fronts. Firstly, how different are V-wall collisions from single inclined-wall collisions and how can well-established flow dynamics associated with the latter be tapped to explain the former's behaviour? Secondly, to what extent do vortex-ring Reynolds number and included-angle influence the resulting collision behaviour, circulation levels and vortex-core trajectories? Last but not least, how do the key flow mechanisms underpinning the present experimental observations compare to earlier findings on inclined-wall or round cylinder based collisions?

To address these questions, laser-induced fluorescence (LIF) visualizations and time-resolved particle-image velocimetry (TR-PIV) measurements were utilized to reveal more details. Similar experimental approaches had already been used by the authors previously in unravelling pertinent details on inclined-wall and round-cylinder based vortex-ring collisions [New *et al.* (2016); New & Zang (2017)]. From the perspectives of engineering applications, these experimental evidence will also provide more flow insights into how continuous or synthetic impinging jet flow behaviour (of which vortex-rings can be treated as their most fundamental flow entity) could be further improved in terms of providing more uniform and efficient heat transfer functions for non-uniform surface geometries.

2. Experimental setup

All experiments were conducted in the same water-tank based experimental setup as described in New *et al.* (2016) and New & Zang (2017), and hence only a brief description will be provided here. With reference to Fig. 1, discrete circular vortex-rings were generated via sudden impulses from a piston to push water out of a nozzle. The piston was located within a stainless-steel round tube with an internal diameter of 20mm, the latter of which was attached to a circular Plexiglas attachment with a similarly sized hole. A cylindrical dye port was designed within the circular attachment such that fluorescent dye could be released uniformly into the working fluid through a 1mm wide built-in circumferential slit by a gravity-fed dye release system. Lastly, a d=20mm inner-diameter circular nozzle was fixed to the circular attachment, where a "cylindrical slug" of water exited from it and into the quiescent water. Depending on the viewing requirements of the experiments, thin 0.09mm matt black adhesive paper was applied either on one or both of the V-wall inner surfaces to minimize laser reflections during the experiments. The vortex-ring Reynolds numbers investigated here are approximately $Re=Ud/\nu$=2000 and 4000 where U and ν are the piston mean velocity and kinematic viscosity of water at working conditions, respectively), where they correspond to $Re_\Gamma = \Gamma/\nu$=2500 and 5000, respectively, indicating that the vortex-rings are generally laminar. All vortex-rings were produced with the stroke length held at L=30mm throughout the study, resulting in a constant stroke ratio of L/d=1.5. This stroke ratio is significantly smaller than the critical L/d=3.6, above which trailing-jets would be produced behind the vortex-rings [Gharib *et al.* (1998)]. Circulations estimated from TR-PIV measurements for the Re=2000 and 4000 vortex-rings here are approximately Γ=0.0025 and $0.050m^2/s$, respectively. These values compare well with studies by Weigand & Gharib (1997) and Couch & Krueger (2011). For instance, the circulation of the Re=1650, L/d=0.87, vortex-ring in Weigand & Gharib (1997) was estimated to be around $0.00162m^2/s$. Additionally, normalized circulations for Re=2000, L/d=0.75, vortex-rings in Couch & Krueger (2011) are approximately $\Gamma/(dU_{max})$=0.8 at about 2-3 diameters above the collision surface. This is compared to a normalized circulation value of approximately

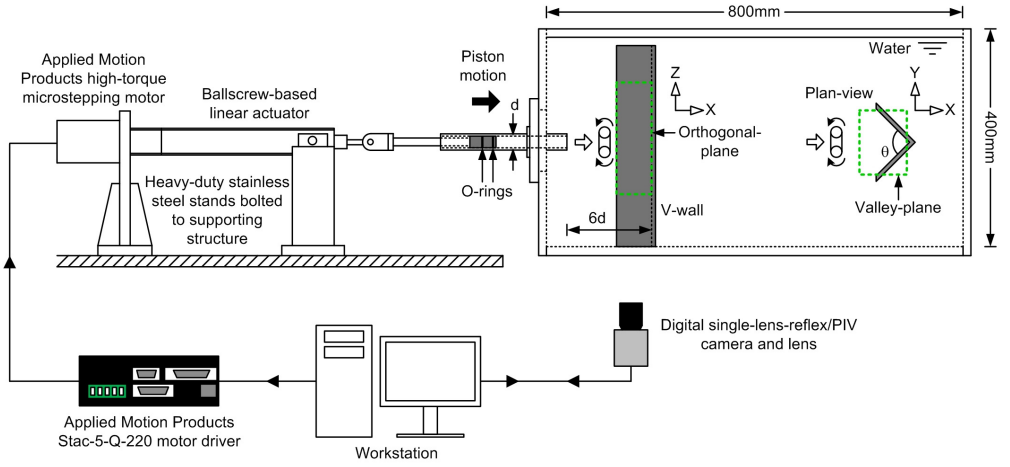

Figure 1: Schematics of the piston-based, "cylindrical-slug" vortex-ring generator and experimental apparatus, where they are very similar to those used by New *et al.* (2016) and New & Zang (2017).

$\Gamma/(dU_{max})$=0.96 here. Considering the significantly larger stroke-ratio used in the present study as compared with these earlier studies, circulations of the present vortex-rings are comparable with these earlier studies. Additionally, the vortex-ring aspect-ratios are estimated to be d_0/σ=2.10 and 2.95 at Re=2000 and 4000, respectively, where d_0 is the vortex-ring core-to-core diameter and σ is the vortex-ring core diameter as shown in Fig. 2(a). Last but not least, vortex-ring profiles are compared to those approximated using Gaussian functions [Orlandi (1993), Cheng *et al.* (2010)] and observed to be Gaussian-like. There are good agreements in the peak velocities, though velocity decays are observed to be faster in the experimental results compared to an idealized Gaussian distribution.

LIF visualization and TR-PIV measurement procedures were similar to the authors' earlier studies. For 2D LIF visualization, fluorescein disodium dye was premixed with water and a small amount was released upstream of the circular nozzle just prior to each experiment. A 532nm continuous-wave diode-pumped solid-state (DPSS) laser was used to produce an approximately 1.5mm thick laser sheet with the use of beam-steering mirrors and sheet-forming optics. The laser sheet was positioned horizontally with respect to the setup during the flow visualization experiments and the V-walls orientated vertically or horizontally to allow visualizations along the 'valley-plane' or 'orthogonal-plane', as shown in Fig. 1 as planes highlighted by green dashed-lines. Based on the present coordinate system, the valley- and orthogonal-planes are aligned with the XY- and XZ-planes respectively. A remotely-controlled 1920 × 1080 pixels digital single-lens-reflex camera with a 50mm, *f*1.4 lens was then used to capture the visualized flow behaviour through 30 frames-per-second video-recordings. As the results will show later, the present vortex-ring collision scenarios would lead to significantly different flow developmental time-spans along the valley- and orthogonal-planes when the Reynolds number and/or included-angle vary. Hence, to better highlight the key vortex structures and behaviour associated with each particular configuration, visualization images taken at different timings will be presented instead of presenting them at the same timings regardless of the exact configuration. For TR-PIV experiments, the same DPSS laser was used but with an IDT grayscale high-speed camera capable of up to 1000 frames-per-second instead. The high-speed camera has a resolution of 1024 × 1024 pixels and was

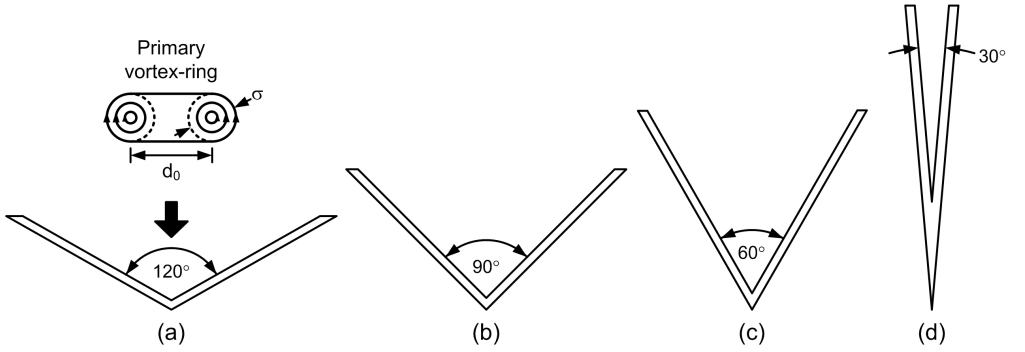

Figure 2: Four V-wall configurations used in the present vortex-ring collision study, where the included-angle, θ, ranged from 120° to 30° at 30° intervals.

set to capture sequential particle-images at 250 to 350 frames-per-second, depending on the vortex-ring Reynolds number. It should be noted that the camera captured particle-images associated with half of the symmetrical flow fields along the orthogonal-plane, as the flow developments occurred over significantly larger distances along this plane. In contrast, a smaller measurement window was used along the valley-plane, since the flow structures and developments were constrained within smaller regions by the physical boundaries of the V-walls. All time-series particle-images were post-processed based on similar procedures adopted by New *et al.* (2016) and New & Zang (2017), and readers are advised to refer to them for more procedural details and uncertainty levels. Last but not least, it should be noted that since the LIF visualizations and TR-PIV measurements were captured at different framerates and hence temporal resolutions, the results presented here were selected such that their timings for the same configuration and instance are as close to each other as possible.

3. Results and Discussion

3.1. *Vortical developments along valley-plane*

Before the results for the present study are presented, it will be worthwhile to briefly recall the flow dynamics associated with laminar vortex-rings colliding normally with a flat-wall first. As observed in an earlier study [New *et al.* (2016)], a Re=2000 primary vortex-ring flattens with an increase in the vortex-ring diameter shortly after it collides with the wall. Subsequently, under the effects of an adverse pressure gradient, the increasingly larger primary vortex-ring leads to the first wall boundary layer separation that produces a secondary vortex-ring with an opposite rotational sense. Thereafter, the secondary vortex-ring leapfrogs over and gets entrained within the inner confines of the primary vortex-ring. At around the same time, the primary vortex-ring produces a second wall boundary layer separation and hence, tertiary vortex-ring. Similar to the secondary vortex-ring, the tertiary vortex-ring may subsequently get entrained by the primary vortex-ring, depending on the primary vortex-ring configuration.

Figures 3 to 6 show instantaneous time-sequenced LIF visualizations for the Re=2000 vortex-ring colliding with the four different V-walls, where they were taken with the camera facing the XY-plane (i.e. valley-plane). Note that flow images at short time-intervals are presented here for a first-hand qualitative appreciation of the underlying flow dynamics. Non-dimensionalized timings where τ=tU/d, similar to that adopted by Couch & Krueger (2011) and New *et al.* (2016), have also been used for the sake of

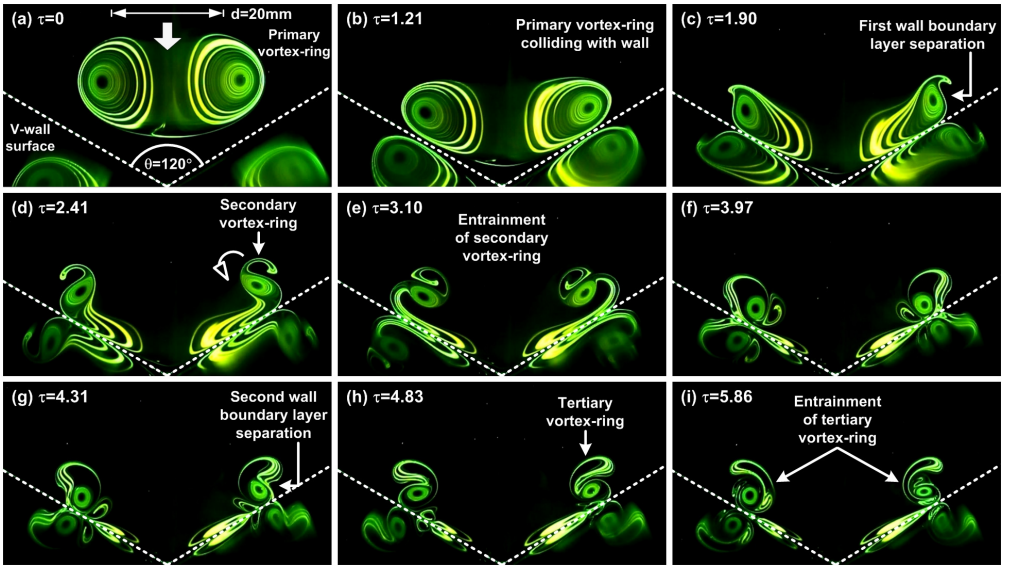

Figure 3: Time-sequenced LIF images of a Re=2000 vortex-ring colliding upon the θ=120° V-wall. General flow behaviour resembles that of a flat-wall collision, except that entrainment and merging of secondary and tertiary vortex-ring cores by the primary vortex-ring cores are more accentuated.

consistency. The flow images are oriented such that the primary vortex-ring is translating downwards and towards the walls, and while reflections of the vortex-ring and collision processes can be seen on the V-wall surfaces, they do not impede flow interpretations. White dashed-lines are used to indicate the V-wall surfaces and length-scales based on the d=20mm nozzle diameter are provided. The latter will be useful in appreciating and comparing the rapid changes to the various vortex-core sizes under certain conditions qualitatively.

Similar to the study conducted by New & Zang (2017), it has to be highlighted that careful alignments between the vortex-rings and the V-walls are crucial towards achieving satisfactorily symmetrical and well-defined flow details, especially for smaller included-angles. Furthermore, it should also be noted that the effective wall inclination angles (i.e. relative to the image horizontal here) for the θ=30°, 60°, 90° and 120° V-walls here are equivalent to those for the θ=75°, 60°, 45° and 30° inclined walls studied earlier (New *et al.* (2016)). Hence, it will be logical to draw comparisons between the results captured in the present study with those by New *et al.* (2016) previously and infer where appropriate. Lastly, it should also be highlighted that the first flow images in Figs. 3 to 6 are associated with primary vortex-rings that are not yet discernibly distorted by its proximity to the wall and taken as initial points-of-reference in terms of time and descriptions of the observed flow dynamics.

Starting with the θ=120° V-wall shown in Fig. 3, where the physical configuration is closest to that of a flat-wall (i.e. θ=180°), distortions to the primary vortex-ring cores and expansion of the ring diameter shortly after the collision unsurprisingly resemble closely to those observed for flat-wall collisions (see Movie 1). Comparing with New *et al.* (2016), the primary vortex-ring diameter does not increase as much as the case for flat-wall collisions after collision, as it is constrained by the V-wall here. Subsequently, wall boundary layer separation under adverse pressure gradient caused by the presence

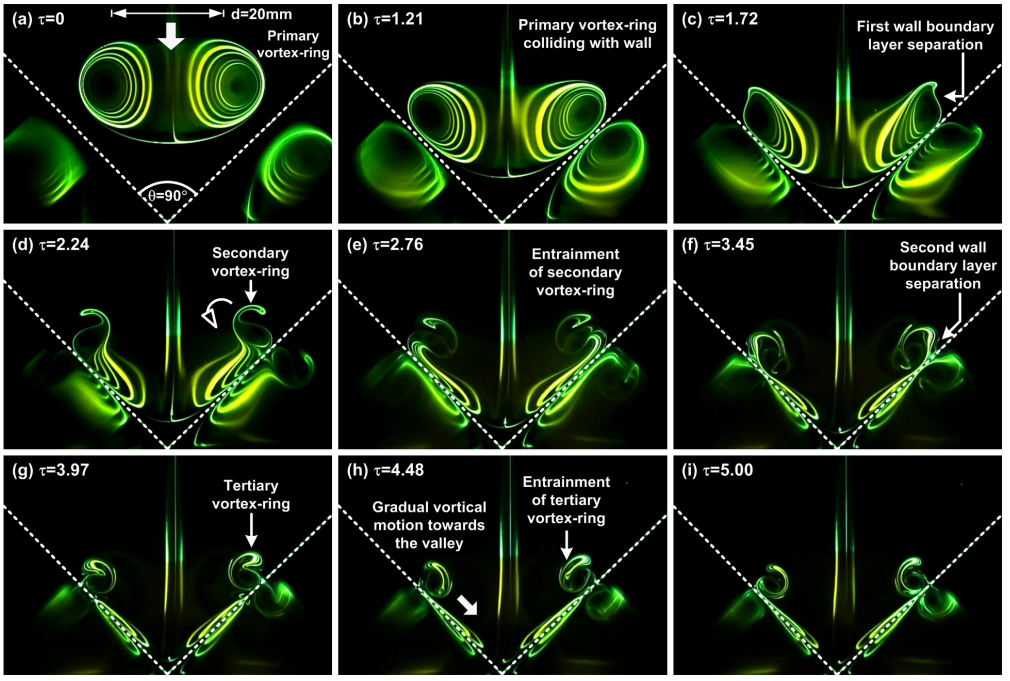

Figure 4: Time-sequenced LIF images of a Re=2000 vortex-ring colliding upon the θ=90° V-wall. Flow developments remain relatively similar to that observed for θ=120° V-wall collision, although the primary vortex-ring cores entrain the secondary and tertiary vortex-ring cores more rapidly now.

of the primary vortex-ring leads to the formation of secondary vortex-ring cores, as well as their entrainment by the primary vortex-ring shortly after the collision [see Figs. 3(a)-(e)]. Unlike flat-wall collisions though, the secondary vortex-ring cores merge with the primary vortex-ring cores more rapidly once they are within the confines of the latter [see Figs. 3(f)-(h)]. A second wall boundary layer separation occurs during the entrainment of the secondary vortex-ring cores and leads to the formation of weak tertiary vortex-ring cores, which get ingested by the primary vortex-ring cores as well [see Figs. 3(g)-(i)]. It should be highlighted that the entrainment process is visually more accentuated even for this wall with a relatively large included-angle, as compared to flat-wall collisions. Furthermore, the primary vortex-ring cores convect slightly towards the vertex of the valley after the preceding flow developments, presumably under flow inertia. As the included-angle reduces to θ=90° as shown in Fig. 4, the vortical changes are similar to those observed for the θ=120° V-wall collision earlier on, though the entrainment and merging of the secondary and tertiary vortex-ring cores by the primary vortex-ring are now more rapid (see Movie 2).

At this point, it should not come as a surprise that the above-mentioned behaviour becomes even more intense as the included-angle reduces to θ=60° (see Movie 3), as shown in Fig. 5. This is particularly the case for the entrainment of secondary and tertiary vortex-ring cores by the primary vortex-ring cores, and as well as the higher rates at which the physical sizes of the various vortex-ring cores are reduced as the flow develops. However, what is more interesting with this configuration is that only the secondary vortex-ring cores merged with the primary vortex-ring. In this case, the entrained tertiary vortex-ring cores do not merge with the primary vortex-ring cores

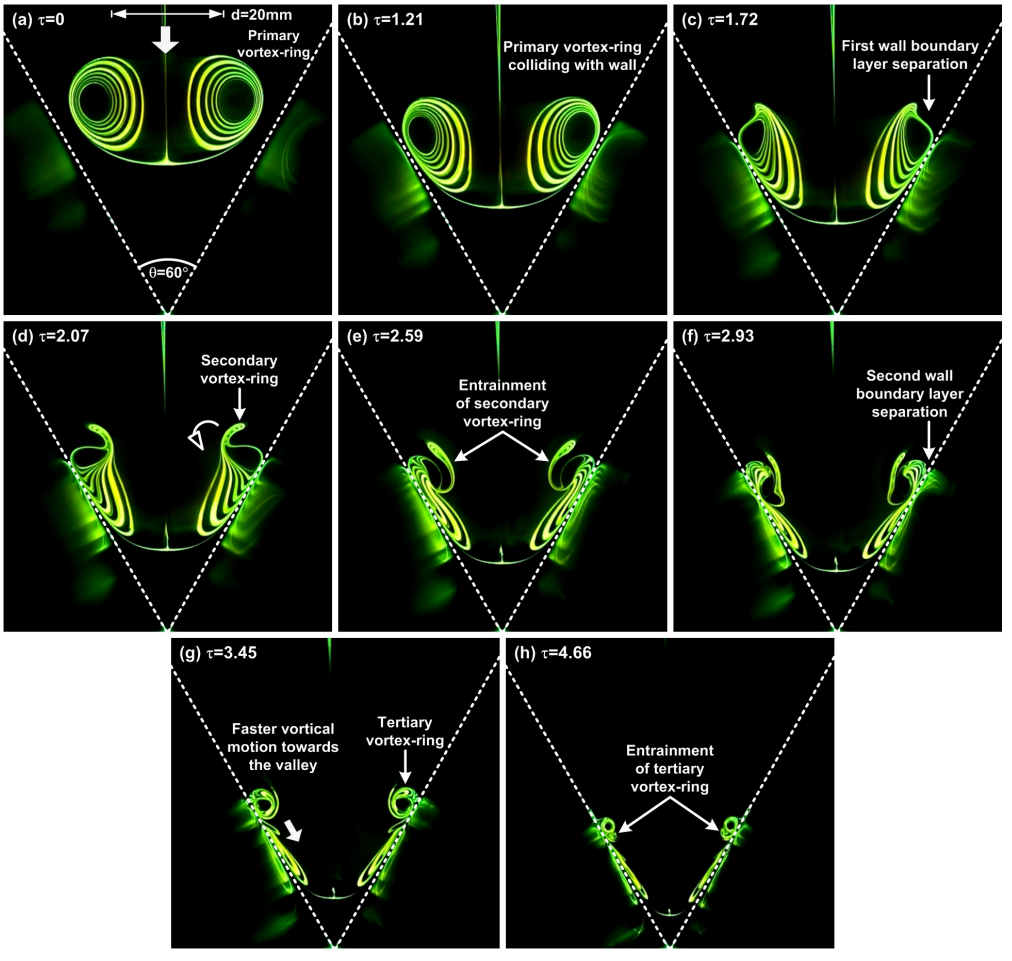

Figure 5: Time-sequenced LIF images of a Re=2000 vortex-ring colliding upon the θ=60° V-wall. Note the increased rate at which the secondary vortex-ring cores are being ingested by and merged with the primary vortex-ring cores and reduction in vortex-core sizes.

but continue to convect down along the walls [see Figs. 5(g)-(h)]. And if the included-angle reduces further to θ=30°, the flow behaviour becomes more intriguing (see Movie 4). Firstly, the secondary vortex-ring cores do not merge with the primary vortex-ring completely after they are entrained by the latter. Instead, part of it convects past the primary vortex-ring cores and continues to convect along the walls towards the vertex of the valley [see Figs. 6(e)-(g)]. At the same time, tertiary vortex-ring cores can be observed to form from a second boundary layer separation. Unlike the secondary vortex-ring cores however, the tertiary vortex-ring cores are completely entrained by and merged with the primary vortex-ring cores [see Figs. 6(f)-(g)]. Subsequently, both the primary and secondary vortex-ring cores move towards the vertex of the valley, while shrinking in physical sizes at the same time.

From the preceding visualization results, it can be surmised that the use of an increasingly smaller included-angle produces a few interesting alterations to the typical flow behaviour established for flat-wall collisions. Firstly, the secondary vortex-ring cores

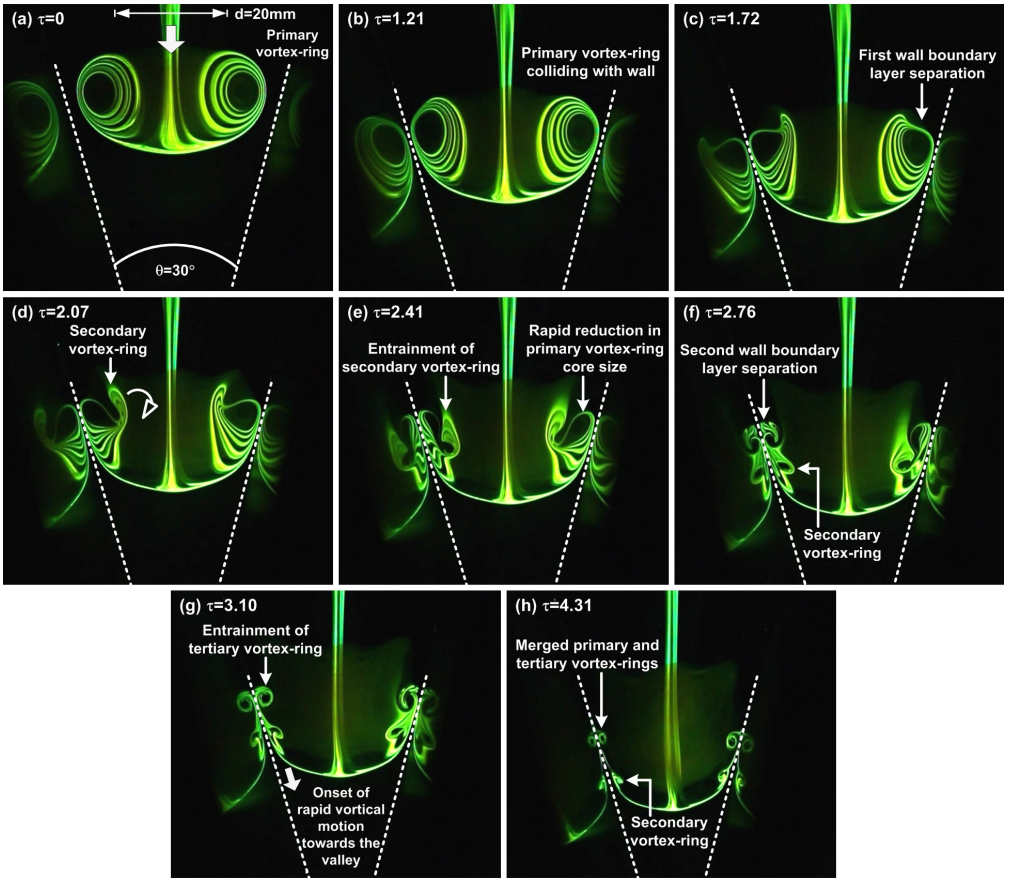

Figure 6: Time-sequenced LIF images of a Re=2000 vortex-ring colliding upon the θ=30° V-wall. Note the continuing passage of the secondary vortex-ring towards the valley after it has been entrained by the primary vortex-ring, as well as the drastic reductions in all the vortex-core sizes.

are gradually able to escape being completely ingested by and merged with the primary vortex-ring cores after their entrainment as the included-angle decreases. Secondly, the secondary vortex-ring cores subsequently interact more with boundary layer ahead of the primary vortex-ring (i.e. along the wall regions closer to the vertex of the valley). Lastly, the reduction in the various vortex-ring core sizes increases rapidly as the included-angle becomes smaller. In fact, this observation indicates that these vortex-ring structures undergo significant stretching effects and movements out of the valley-plane in opposite directions (i.e. symmetrically along the orthogonal-plane), due to physical constraints imposed by the V-walls. As visualization results along the orthogonal-plane will show later, that is indeed be the case.

To complement the scalar dye-based flow visualizations and for a more quantitative appreciation of the flow changes, vorticity maps of the preceding flow scenarios obtained through TR-PIV measurements are presented in Figs. 7 and 8. For the sake of brevity, only the results associated with θ=120° and 30° V-walls are shown here, as they reveal the most significant flow changes produced by a drastic reduction in the included-angle. Figures 7 shows that the collision behaviour of primary vortex-ring, formations

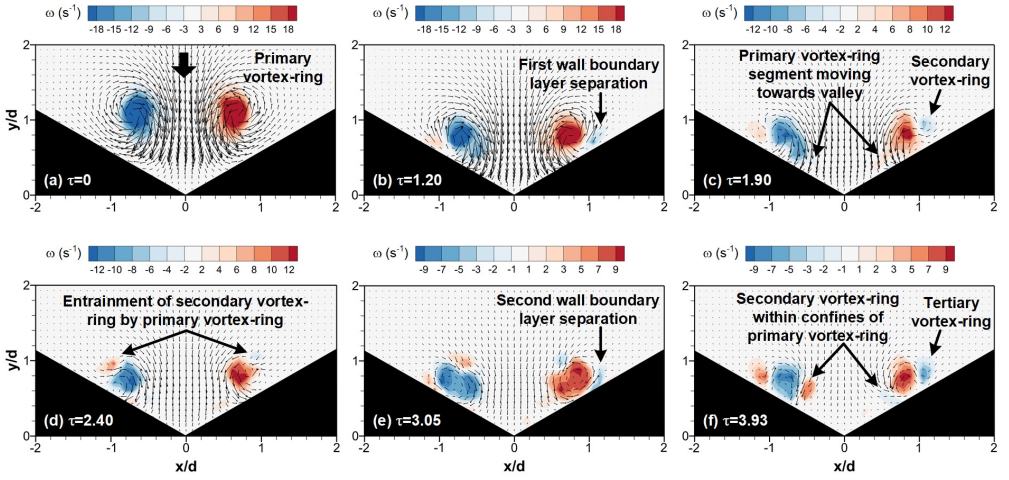

Figure 7: Time-sequenced vorticity maps of a Re=2000 vortex-ring colliding upon the θ=120° V-wall. Note that vortical changes such as wall boundary layer separations, formations of secondary and tertiary vortex-ring cores and their subsequent entrainment by the primary vortex-ring are captured.

of secondary and tertiary vortex-ring cores and their subsequent entrainments by the primary vortex-ring cores for the θ=120° V-wall are successfully captured and compare well with the earlier visualization images. Due to the need to cover a certain measurement region size for the translating vortex-ring during the TR-PIV measurements, as well as the fact that the tertiary vortex-ring cores become increasingly physically smaller as the included-angle reduces [see Figs. 5 and 6], the current measurement resolution is not sufficiently high to capture the tertiary vortex-ring cores for the θ=60° and 30° V-walls here. Nonetheless, the vorticity results for the θ=30° wall, as shown in Figs. 8, demonstrate quantitatively the intense interactions between the various vortex-ring cores, especially during the entrainment process. Lastly, velocity vectors depicted in these results also show that flow inertia from the primary vortex-ring provides the flow momentum that keeps the various vortex-ring cores moving towards the vertex of the valley, even as they are engaged in mutual interactions. Hence, unlike the case for flat-wall collisions, the presence of a background translation velocity while vortical changes aremain confined renders the present collision behaviour more three-dimensional and complex.

3.2. *Effects of vortex-ring Reynolds number*

It is observed during the present study that increasing the Reynolds number has a direct impact upon the behaviour of the secondary and tertiary vortex-ring cores after they leapfrog past the primary vortex-ring cores when the included-angle is small. Recall the case for flat-wall collisions, where they will remain within the confines of the primary vortex-ring and transit to incoherence thereafter, an increase in Reynolds number primarily serves to accelerate the flow developments and transition to incoherence [Walker *et al.* (1987); Verzicco & Orlandi (1994); Swearingen *et al.* (1995); Naitoh *et al.* (2001); Cheng *et al.* (2010); New *et al.* (2016)]. In the present flow configuration however, a combination of higher Reynolds number and smaller included-angle (i.e. in particular the latter) are able to lead to formations of new vortex structures and behaviour not observed previously. For θ=120° and 90° V-wall collisions with Re=4000 vortex-rings, key

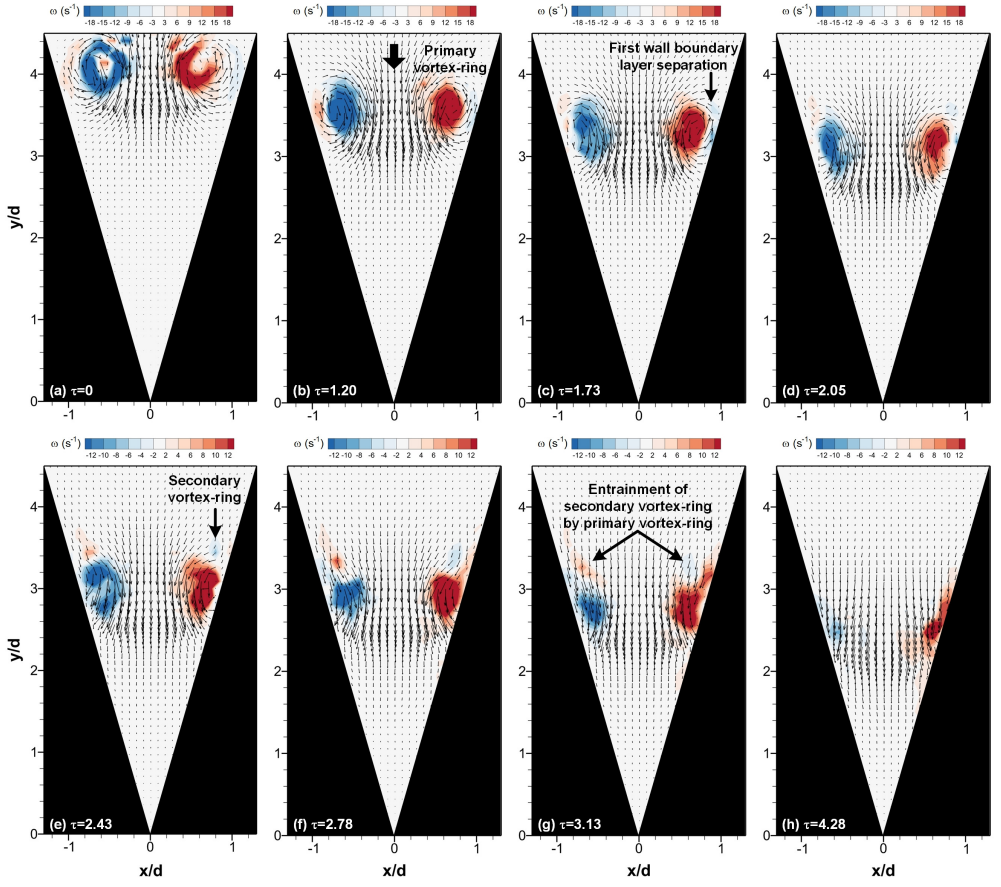

Figure 8: Time-sequenced vorticity maps of a Re=2000 vortex-ring colliding upon the θ=30° V-wall. Similar to observation in Fig. 6, vortical changes and interactions occur very rapidly once the primary vortex-ring collides with the V-wall.

flow developments of the vortex-ring collisions do not differ much from those observed at Re=2000, except being more rapid (i.e. hence, results not shown for the sake of brevity). The more notable difference will be that a third boundary layer separation occurs after the formation of the tertiary vortex-ring to produce a second set of tertiary vortex-ring cores. Together with the secondary and first set of tertiary vortex-ring cores, the second set of tertiary vortex-ring cores gets ingested by and merged with the primary vortex-ring cores after entrainment. For θ=60° and 30° V-wall collisions with Re=4000 vortex-rings however, other than the expected boundary layer separations after the collision that produce the secondary and tertiary vortex-ring cores, their rapid entrainment by the primary vortex-ring cores also leads to further intriguing observations. In particular, when the entrained secondary and/or tertiary vortex-ring cores do not merge with the primary vortex-ring cores, they produce previously unseen vortex structures when they leapfrog and impinge upon the walls ahead of the primary vortex-ring cores.

Take for instance, as can be seen in Fig. 9 for the θ=60° wall, the impingement of the tertiary vortex-ring cores along the wall ahead of the primary vortex-ring cores after the former have been entrained by the latter leads to the interesting appearance of small mushroom-shaped vortex-dipoles in Fig. 9(i). Playbacks of LIF video recordings

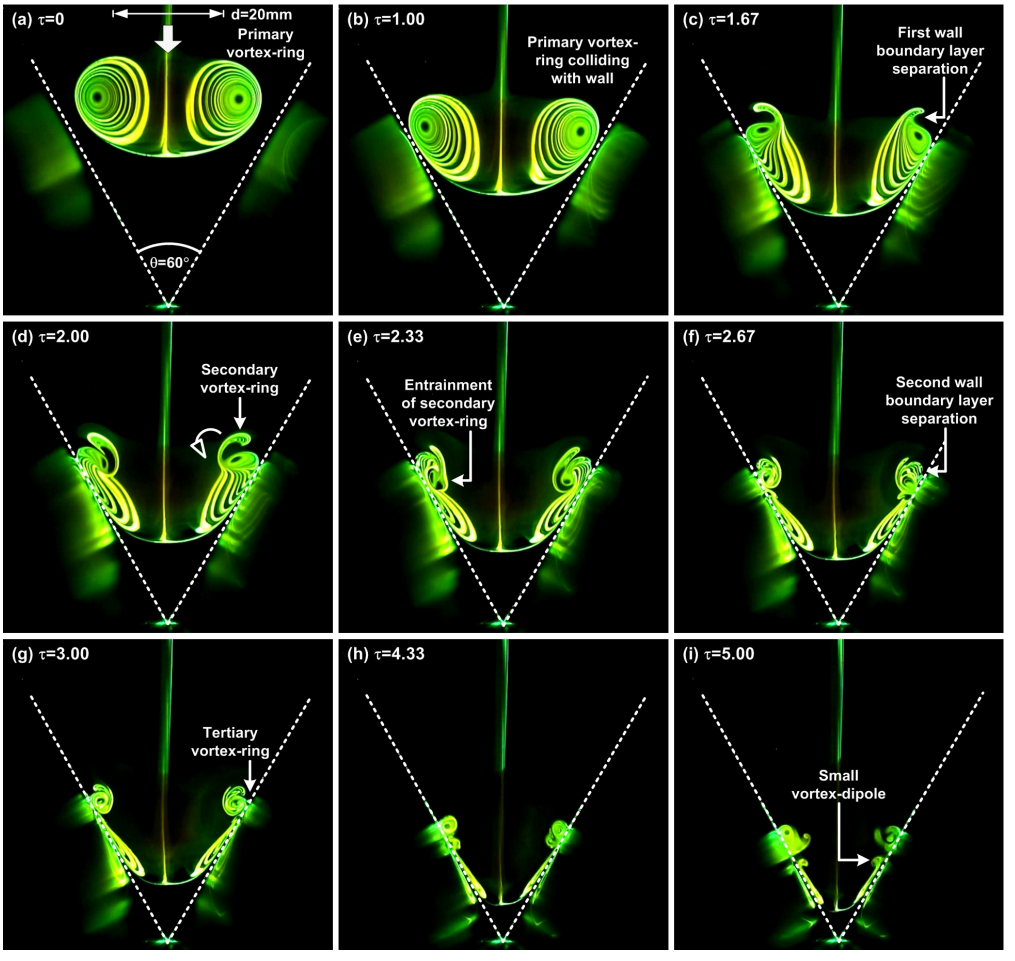

Figure 9: Time-sequenced LIF images of a Re=4000 vortex-ring colliding upon the θ=60° V-wall. Interesting formations of small-scale vortex-dipoles upstream by the tertiary vortex-ring cores and a wall-separated vortex upstream of the primary vortex-ring cores can be seen here.

associated with Fig. 9 suggest that the presence of the tertiary vortex-ring cores along the V-wall surfaces (after the preceding behaviour) leads to adverse pressure gradients upstream of the primary vortex-ring cores. This in turn produces wall boundary layer separations and wall-separated vortex structures that possess rotational senses that are opposite to those of the tertiary vortex-ring cores, much like what happens when the primary vortex-ring cores lead to the formation of secondary vortex-ring cores. Subsequently, each tertiary vortex-ring core pairs up with each of these opposite-signed vortex structures along each V-wall surface to form a small-scale vortex-dipole which convects towards the vertex of the valley under flow inertia. For the smallest included-angle of θ=30°, the primary vortex-ring cores encounter the wall soon after they are formed, which leads to comparatively earlier formation of the secondary vortex-ring cores (i.e. τ=1.33 and 1.67 for 30° and 60° V-walls, respectively) [see Figs. 10(a)-(d)] and their entrainment by the primary vortex-ring cores (i.e. τ=1.67 and 2.33 for 30° and 60° V-walls, respectively). Note that more detailed information and analysis on these timings

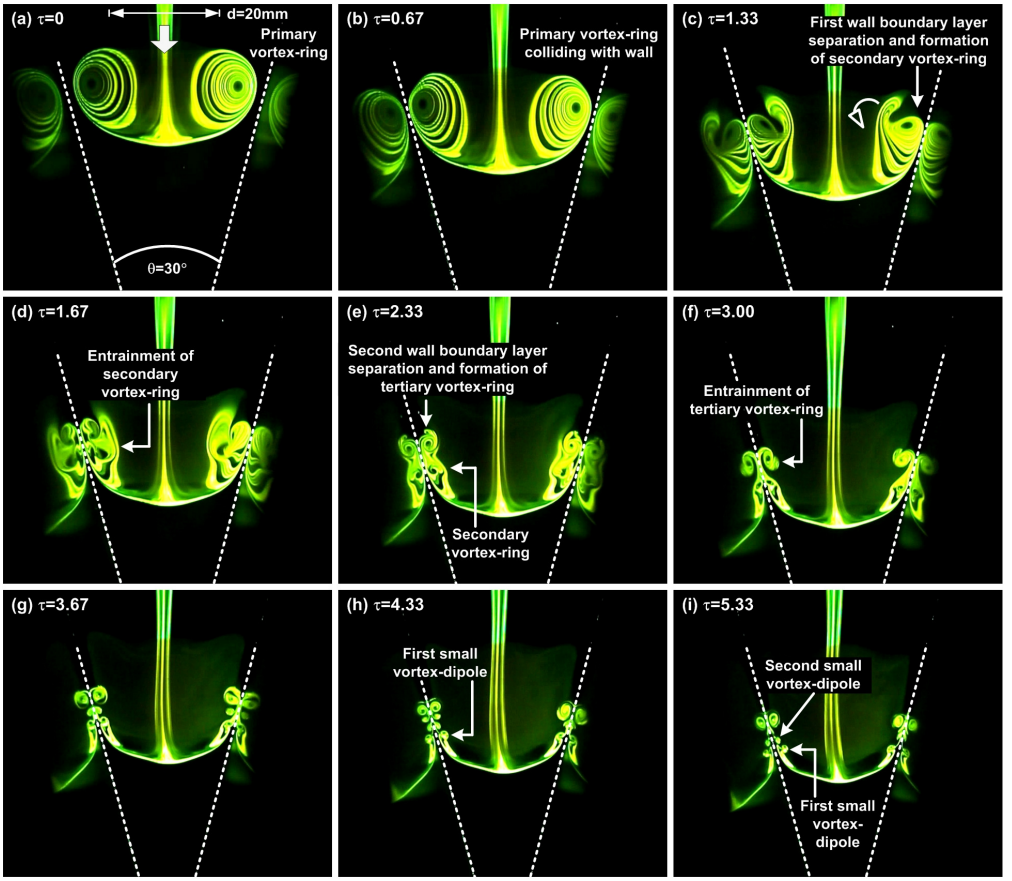

Figure 10: Time-sequenced LIF images of a Re=4000 vortex-ring colliding upon the θ=30° V-wall. Multiple instances of small-scale vortex-dipoles can be observed here, suggesting higher Reynolds number and smaller included-angle to be conducive towards their formations.

will be presented and discussed later. In this case however, the entrainment process distorts both the primary and secondary vortex-ring cores significantly, likely reinforced by the much higher wall shear stresses associated with the more inclined V-wall here. Subsequently, the entrained secondary vortex-ring cores impinge upon the wall after their entrainment and leads to the formation of new wall-separated vortex structures downstream of it, where their formations would be similar to what had been described earlier.

3.3. *Vortical developments along orthogonal-plane*

Flow visualization images taken for Re=2000 vortex-ring collisions but along the orthogonal-plane for θ=120°, 90°, 60° and 30° V-walls are now presented in Figs. 11 to 14, respectively. Note that the laser sheet was aligned along the inner-edge of the valley and XZ-plane, with the camera facing it. Out of the four configurations, the vortex dynamics associated with θ=120° V-wall are visually the clearest and most intricate. Furthermore, flow developments for θ=120° and 90° V-walls appear to be quite different

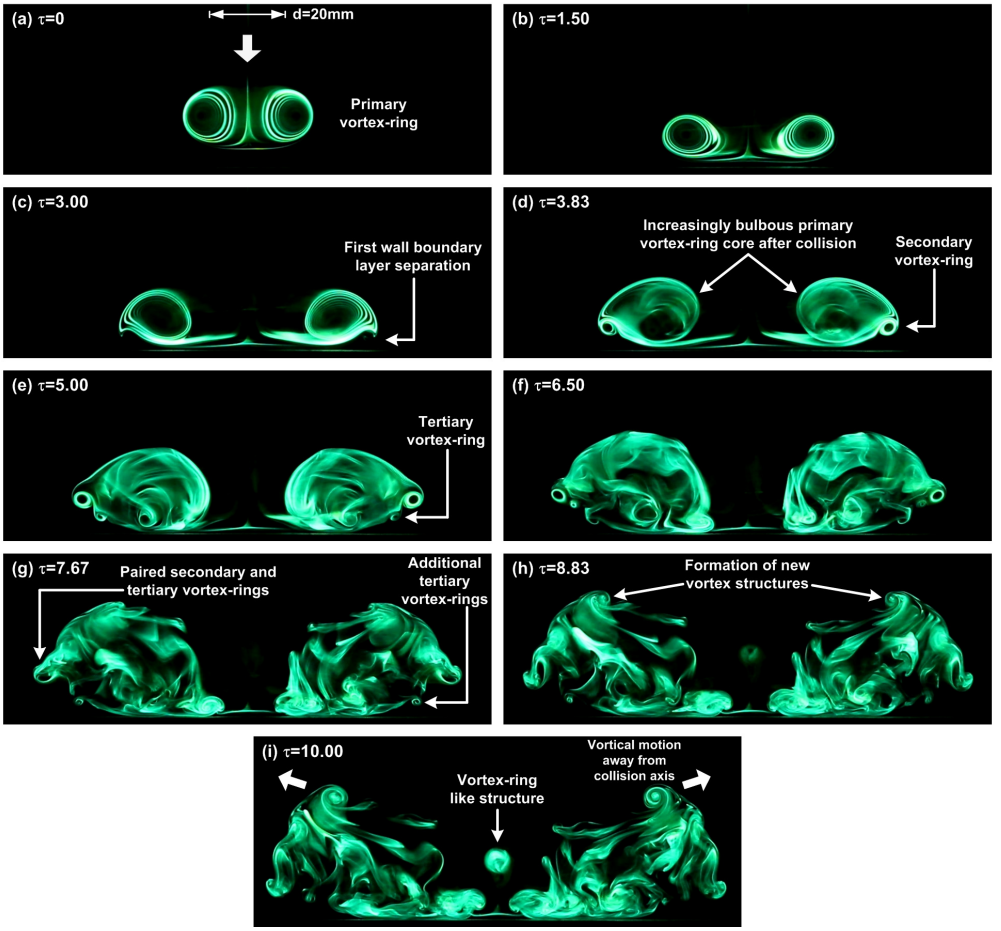

Figure 11: Time-sequenced LIF images taken along the orthogonal-plane for Re=2000 vortex-ring colliding upon the θ=120° V-wall. Formations of secondary and multiple tertiary vortex-ring cores can be observed after the collision, alongside with flow developments that give rise to new vortex structures along the top-side of the primary vortex-ring and a small vortex-ring like structure along the collision axis.

from those of θ=60° and 30° V-walls along this plane. Hence, subsequent discussions will be differentiated between these two sets of included-angles.

To start things off, Fig. 11 shows the primary vortex-ring colliding with the V-wall with its cores moving away from the collision axis (see Movie 5). It should be mentioned that the movements of the primary vortex-ring cores away from the collision axis are more rapid and greater than those observed for flat-wall collisions by New *et al.* (2016) for the same primary vortex-ring initial condition previously. During the same time, the boundary layer separates under adverse pressure gradients caused by the vortex-ring cores outwardly movements to produce secondary vortex-ring cores [see Figs. 11(a)-(d)]. While these are occurring, the primary vortex-ring cores can also be observed to grow increasingly bulbous and incoherent, while multiple instances of increasingly weaker tertiary vortex-rings are produced from additional boundary layer separations [see Figs. 11(e)-(g)]. Subsequently and more interestingly, the flow field reorganizes and coherent vortex structures gradually form along the top peripheral regions of the increasingly

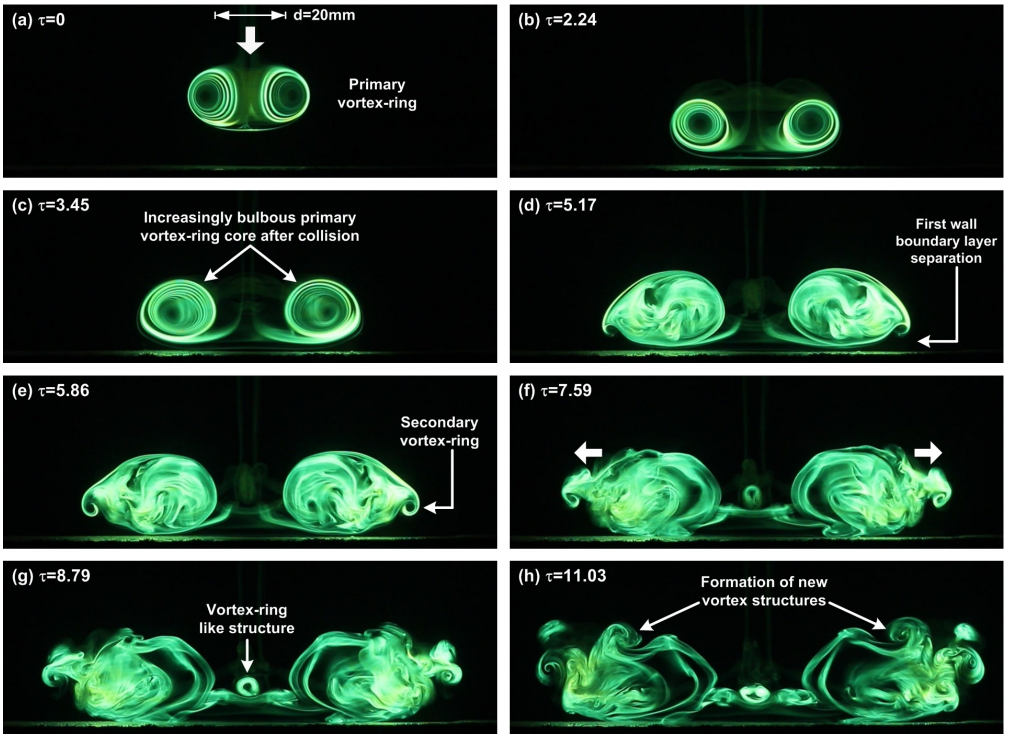

Figure 12: Time-sequenced LIF images taken along the orthogonal-plane for Re=2000 vortex-ring colliding upon the θ=90° V-wall. The flow images depict flow behaviour and structures relatively similar to those observed in Fig. 11, down to the top-side vortex structures and small vortex-ring like structure.

turbulent primary vortex-ring cores [see Fig. 11(h)]. Intriguingly, these vortex structures move away from the collision axis and in doing that, resemble two large-scale mushroom-shaped structures moving away from each other. Of particular interest here will be the formation of a small vortex-ring like structure along the collision axis and approximately $1D$ above the inner-edge [see Fig. 11(i)].

As the included-angle reduces to θ=90° as shown in Fig. 12, the flow behaviour remains largely similar with some notable exceptions (see Movie 6). Firstly, secondary vortex-ring cores form later and only after the primary vortex-ring cores have bulged and become incoherent [see Fig. 12(d)] and secondly, no discernible tertiary vortex-ring cores are observed to form though they could in principle be very weak and did not entrain sufficient fluorescent dye to be observed clearly. Thirdly, the secondary vortex-ring cores appear to pair up with other flow structures as a result of the underlying vortex dynamics and lead to vortex-dipoles forming along the sides of the now largely incoherent primary vortex-ring cores [see Figs. 12(f)-(g)]. Note that these vortex-dipoles are different from the vortex structures that appear along the top peripheral region of the primary vortex-ring cores observed in Fig. 11(h) earlier, as the current ones only appear significantly later as shown in Fig. 12(h). Lastly, the small-scale vortex-ring like structure along the collision axis now forms nearer to the inner-edge at approximately $0.5D$ above it.

If the included angle reduces further to θ=60° and 30° as shown in Figs. 13 and 14 (see Movies 7 and 8), it can be observed that the primary vortex-ring cores bulge and transit to turbulence rapidly even before they come close to the wall inner-edge [see Figs. 13(a)-(e)

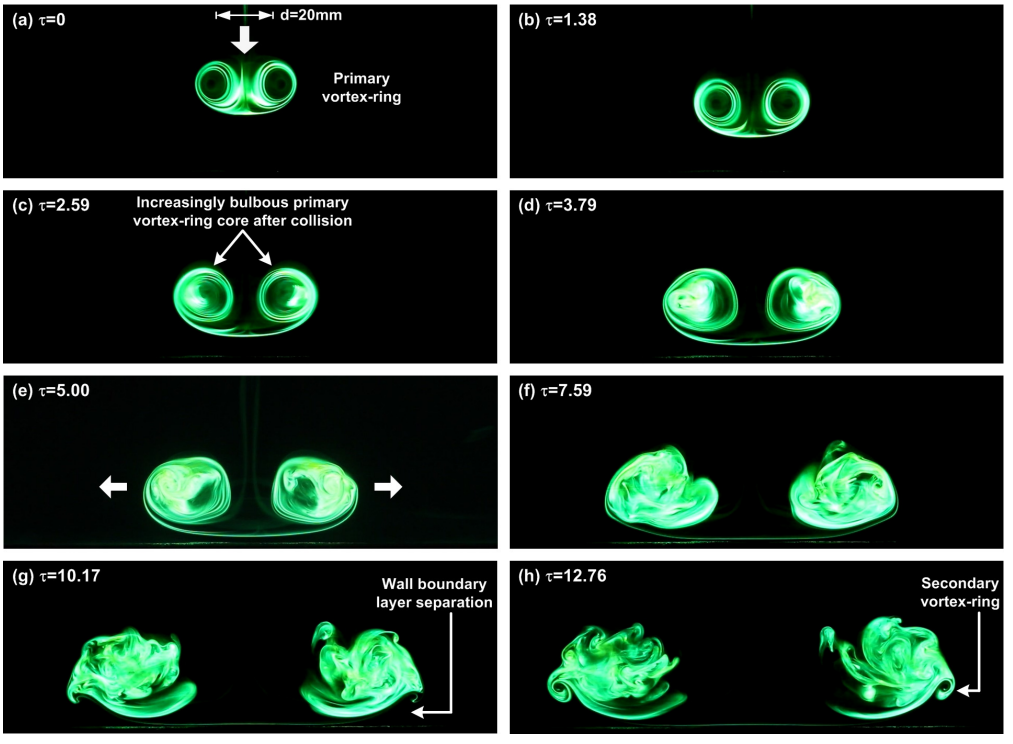

Figure 13: Time-sequenced LIF images taken along the orthogonal-plane for Re=2000 vortex-ring colliding upon the θ=60° V-wall. The primary vortex-ring cores transit to incoherence earlier with no formation of tertiary vortex-ring cores and top-side vortex structures observed.

and 14(a)-(h)]. It should be noted that a small pair of vortex structures can be observed to form above the primary vortex-ring cores in Figs. 13(e)-(f) and 14(c)-(d), likely caused by the earlier formations of the secondary vortex-ring and its entrainment by the primary vortex-ring along the V-wall surfaces which then propagates from the walls towards the orthogonal-plane. However, they appear to merge with the increasingly bulbous primary vortex-ring cores very rapidly after appearing, which will agree with what was observed in the flow visualizations presented in Figs. 5 and 6 earlier. When the primary vortex-ring cores eventually reach the vertex of the valley however, additional wall boundary layer separations occur to produce pairs of vortex structures that resemble very much like the secondary vortex-ring cores observed in Figs. 11 and 12. However, since it has been established earlier on that the secondary vortex-ring forms much earlier along the V-wall surfaces, it stands to argue that these vortex structures are visualizations of the same secondary vortex-ring that are fully formed when primary vortex-ring segments along the orthogonal-plane finally impact upon the wall inner-edge. It would appear at this point that the use of a V-wall with an increasingly smaller included-angle will introduce a correspondingly larger phase lag in the formation of secondary vortex-ring segments along the V-wall surface and wall inner-edge. A smaller included-angle will result in a "narrower" wall and hence, introduce a larger discrepancy in the locations and times at which different primary vortex-ring segments will come into physical contact with the V-wall surfaces and inner-edge. For the present flow conditions, the critical included-angle appears to be approximately between θ=60° and 90°. Returning to Figs. 13 and

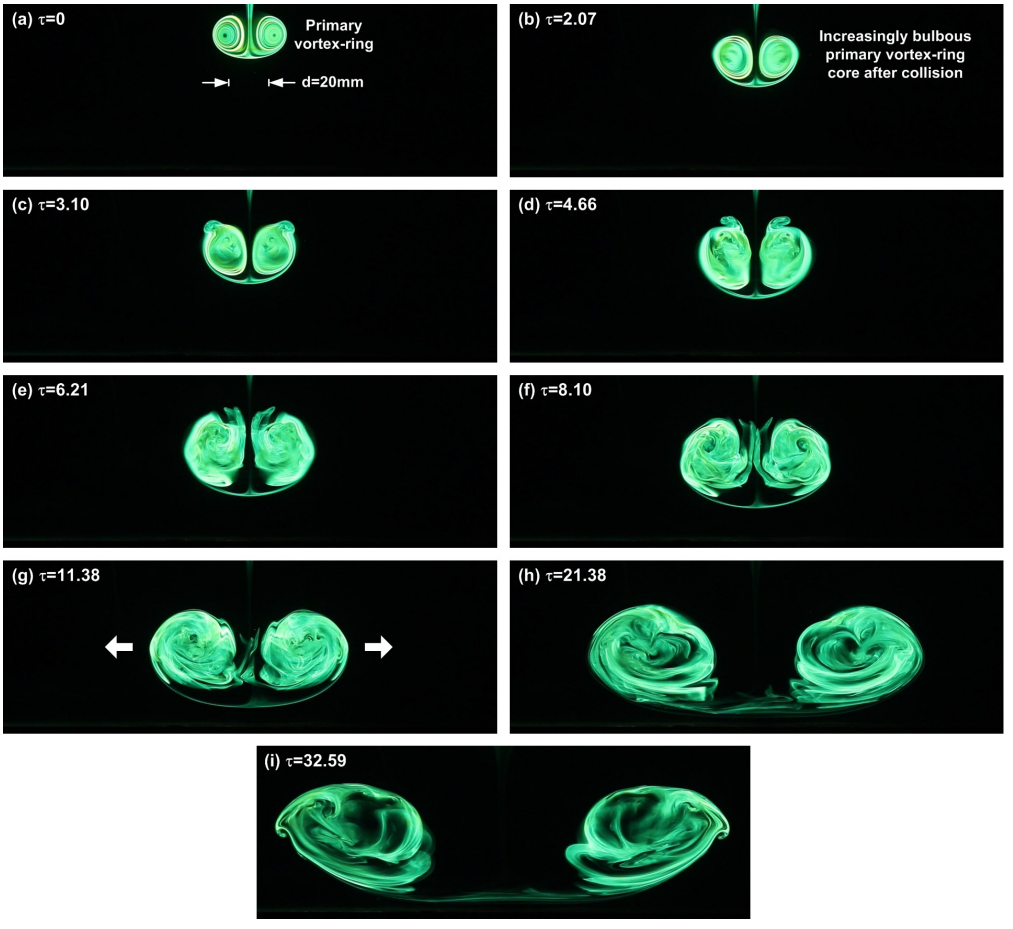

Figure 14: Time-sequenced LIF images taken along the orthogonal-plane for Re=2000 vortex-ring colliding upon the θ=30° V-wall. Images show a behaviour that is similar to that depicted in Fig. 13, except that primary vortex-ring cores become incoherent and secondary vortex-ring cores are formed very shortly after the former collide with the V-wall surfaces. Significant movements away from the collision axis incurred by the primary vortex-ring cores can also be clearly observed here.

14, no discernible tertiary vortex-ring cores and vortex-dipoles like those observed for larger included-angles result from these collision scenarios, and certainly no small vortex-ring like structures are formed along the collision axis at any point during these flow visualizations.

The behaviour of the primary vortex-ring cores when the included-angle reduces to θ=60° and smaller may be better appreciated if one considers earlier studies by Lim (1989), Verzicco & Orlandi (1994) and Cheng *et al.* (2010) on the dynamics of vortex-ring collisions on inclined-walls. Their studies revealed that such collisions lead to dissimilar stretching along the vortex-ring filament and compression of bi-helical lines. These behaviour in turn produce circumferential flows that move from the vortex-ring segment that collides with the inclined-wall first, towards the diametrically-opposite vortex-ring segment that collides with the inclined-wall later. With that in mind, consider also the fact that each of the inclined surfaces associated with the θ=60° and 30° V-walls here have

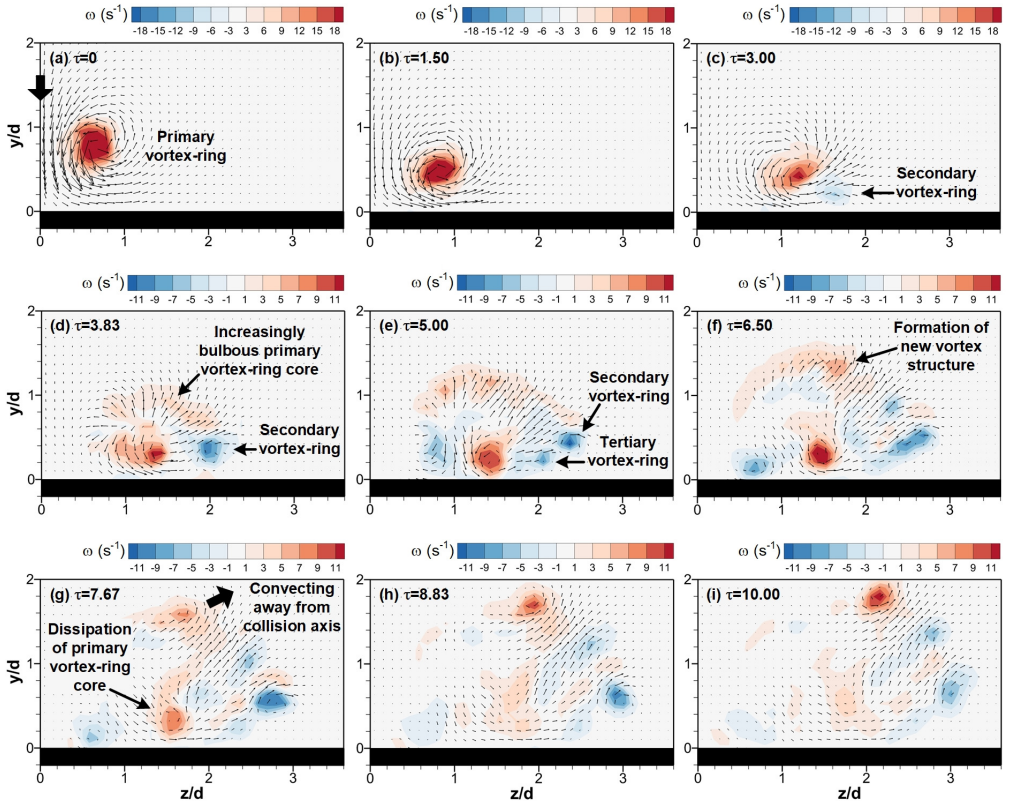

Figure 15: Time-sequenced TR-PIV vorticity distributions for Re=2000 vortex-ring collision upon the θ=120° V-wall along the orthogonal-plane. Quantitative evidence for the secondary and tertiary vortex-ring core formations, new vortex structure along the topside of the primary vortex-ring core and its movement away from the collision axis can be observed here and agree with flow visualizations in Fig. 11.

the same effective inclinations as the θ=60° and 75° inclined-walls investigated by New *et al.* (2016) respectively, which can certainly be treated as highly-inclined and produce very significant circumferential flows. Inferring from results obtained by the above-mentioned studies, circumferential flows from the collided primary vortex-ring segments (i.e. starting from both V-walls surfaces) towards segments that have not collided with the V-wall surfaces (i.e. ending along the present orthogonal-plane) are expected to be very significant at small included-angles. It should be noted that earlier results by New *et al.* (2016) had demonstrated the significant extent of circumferential flow when the same vortex-ring collides with an inclined-wall, so the presence of two inclined surfaces that formed each V-wall will only serves to accentuate the circumferential flows. As a result, severe compression of vortex lines occurring right along the orthogonal-plane will account for the rapid transition towards flow incoherence.

Due to the marked increase in the rate at which the primary vortex-ring evolves and transits into incoherence under the present scenario, scalar dye might have not tracked all the key flow developments. To understand better, vorticity distributions from TR-PIV measurements along the orthogonal-plane are now presented in Figs. 15 to 16. Note that since earlier flow visualization results have shown that the general flow behaviour

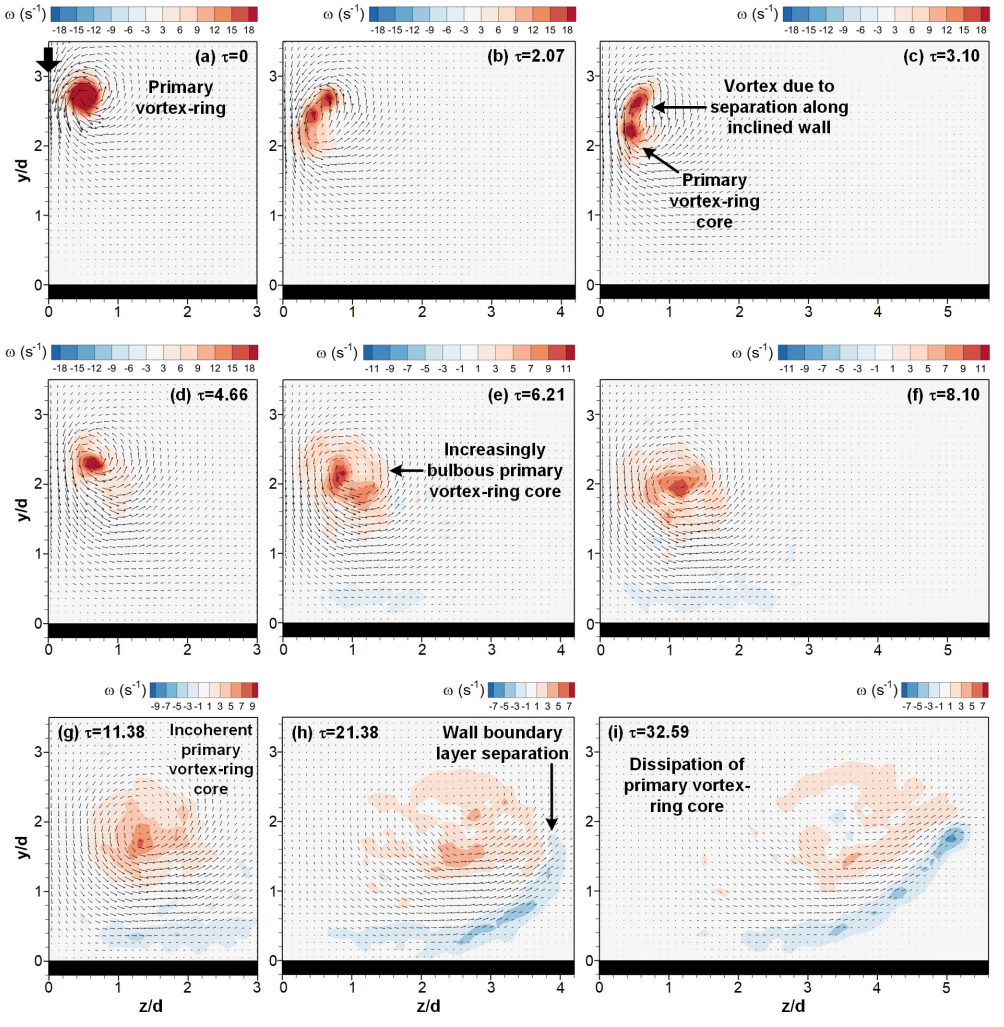

Figure 16: Time-sequenced TR-PIV vorticity distributions for Re=2000 vortex-ring collision upon the θ=30° V-wall along the orthogonal-plane. Flow structures and behaviour resemble closely to the corresponding flow visualizations in Fig. 18 and those observed in the vorticity maps of its θ=60° counterpart in Fig. 14.

can be differentiated between $\theta \leqslant 60°$ and $\theta \geqslant 90°$ V-walls, only the results for θ=120° and 30° V-walls will be shown here for the sake of brevity. In Figs. 15 where results for θ=120° V-wall are shown, the vorticity maps depict flow developments that are in good agreement with what had been observed during the flow visualizations in Figs. 11 and 12, further reinforcing the notion that the flow dynamics do not differ much between these two configurations. Not only do these results show the primary vortex-ring cores becoming more bulbous and incoherent after the collision, they also successfully captured the formations of the secondary and tertiary vortex-ring cores [see Figs. 15(d)-(e)]. In particular, they show that the new vortex structures that form along the top peripheral region of the primary vortex-ring are likely to be part of the latter as it undergoes vortical changes [see Figs. 15(f)]. The movements of these new vortex structures away from the collision-axis have also been captured [see Figs. 15(g)-(i)]. On the other hand,

the small vortex-ring like structures along the collision-axis are not captured in these results, presumably due to their very small physical sizes and highly transient nature.

In contrast, Fig. 16 shows the primary vortex-ring colliding upon the θ=30° V-wall and transiting towards incoherence at some distances away from the wall inner-edge, similar to the flow visualizations presented in Figs. 13 and 14 earlier. In particular, the vorticity maps successfully captured the early formations of a pair of vortex structures along the topside of the primary vortex-ring cores early into the flow at significant distances away from the wall inner-edge at the bottom, which result in the formation of two vortex-cores of similar rotational senses early into the collisions [see Figs. 16(c)]. Discussions earlier on have indicated that they are cross-sections of the secondary vortex-ring formed by the much earlier wall boundary layer separations along the V-wall surfaces that propagate towards the orthogonal-plane. Subsequent vorticity maps show them merging with the primary vortex-ring cores as one single increasingly incoherent vortical entity impacting upon the inner-edge eventually. Thereafter, wall boundary layers separate along this plane to produce the second instance of secondary vortex-rings.

3.4. *Circulation variations*

In this section, changes to the circulation levels of the primary, secondary and tertiary vortex-ring cores will be presented and discussed. Figure 17 shows non-dimensionalized circulations associated with these vortex structures determined along the valley- and orthogonal-planes plotted against non-dimensionalized times. The circulation levels, Γ, were determined according to the procedures described in New & Zang (2017), where the TR-PIV vorticity fields were integrated over the vortex-core areas through the use of Stokes theorem. It is worth pointing out that though these circulation levels were derived from 2D TR-PIV measurements, they will provide some indicative information on how the included-angle affects the vortex dynamics and structures. The absolute circulation levels were subsequently non-dimensionalized by Γ_0, where the latter is the reference circulation level of the primary vortex-ring after it was fully-formed but before it was influenced by the presence of the V-wall ((in the present study, 2.5d from the apex of the V-walls for θ=120° and 90° V-walls, 3d and 4d for θ=60° and 30° V-walls, respectively). On the other hand, time, t, was non-dimensionalized by Γ_0/d^2 and these non-dimensionalizations are in accordance to vortex-ring studies conducted earlier by Cheng *et al.* (2010, 2014). The approximate times of vortex-ring collisions are indicated as vertical dashed-lines in the plots to better differentiate the circulation changes before and after the collisions.

Figure 17(a) shows the primary and secondary vortex-ring core circulation variations along the valley-plane as the included-angle increases from θ=30° to 120°. At first glance, it can be observed that the primary vortex-ring core circulation becomes increasingly more affected even before colliding with the V-wall as the included-angle decreases. Specifically, it can be seen in Fig. 17(a)(i)-(a)(iii) that reductions in the primary vortex-ring core circulation levels increase as the primary vortex-ring translates towards the θ=90°, 60° and 30° V-walls. In contrast, this is hardly the case for the θ=120° V-wall, where the primary vortex-ring core circulation remains relatively constant before the collision. Such an observation can be attributed to the increasingly more adverse pressure gradients set up by V-walls with progressively smaller included-angles, due to the physical limitations imposed by the enclosed valleys. After the collisions however, primary vortex-ring core circulation decreases dramatically in similar fashion as with vortex-ring collisions upon flat-walls, where a more rapid reduction is associated with a larger included-angle. This circulation reduction is associated with heightened vortex-stretching caused by primary vortex-ring segments continuing to translate towards the

wall inner-edge, as well as other segments translating out of the orthogonal-plane due to the confined boundary. However, it can also be seen that the primary vortex-ring core circulations for θ=90° and 120° V-walls tend to approach a relatively "plateau" level of approximately 20% of the initial value (i.e. before the collision) at $t\Gamma_0/d^2 \approx 6$, where further reductions can be attributed to gradual viscous dissipation.

In contrast, for θ=30° and 60° V-walls, rapid reductions in the primary vortex-ring core sizes meant that it is not possible to determine the primary vortex-ring circulations reliably from the TR-PIV measurements from $t\Gamma_0/d^2 \approx 5.5$ onwards. Nevertheless, together with the experimental results presented earlier, the primary vortex-ring core circulations for θ=30° and 60° V-walls are not expected to demonstrate a "plateau"-like behaviour at any point in time. Instead, all evidences point towards rapid reductions in the circulation level due to stronger vortex-stretching behaviour associated with smaller included-angles. Recall that earlier works by Lim (1989) and New *et al.* (2016) had demonstrated strong circumferential flows along the vortex-ring filament, starting from the vortex-ring segment that first collides with an inclined-wall to the diametrically opposite segment. Lastly, secondary vortex-ring core circulations are significantly lower regardless of the included-angle, staying between approximately 5-10% of the initial primary vortex-ring circulation.

As for the circulation behaviour along the orthogonal-plane as depicted in Fig. 17(b), there are discernible trends as the included-angle varies as well. In particular, similar to the circulation behaviour along the valley-plane discussed above, the circulation behaviour appears to be distinguishable between smaller (i.e. θ=30° and 60°) and larger included-angles (i.e. θ=90° and 120°) here. For θ=30° and 60° V-walls, the primary vortex-ring circulation undergoes a relatively straight-forward gentle reduction after it collides with the V-wall, where a smaller included-angle leads to a smaller reduction. Additionally, it should be noted that it was difficult to reliably estimate the circulation of the secondary vortex-ring cores for the θ=30° V-wall, due to their small physical sizes and resolution limitations in the TR-PIV measurements, even though secondary vortex-ring cores do appear in Figs. 14 and 16. Nonetheless, secondary vortex-ring core circulations are successfully estimated for the θ=60° V-wall and they can be observed to increase once the secondary vortex-ring cores are formed. In fact, the peak circulation level is more than double the initial value.

As for θ=90° and 120° V-walls, while the primary vortex-ring core circulations along the orthogonal-plane reduce rapidly after the collisions as expected, they begin to increase after reaching a minimum value. Having said that, the increments reach a maximum and the circulation levels decrease thereafter. This behaviour has not been observed in vortex-ring collisions upon flat-wall under similar flow conditions (New & Zang (2017)), as well as for θ=30° and 60° V-walls under the current experimental conditions. At this point in time, it is postulated that the differences in the circulation behaviour can be attributed to the rate of vortex compression along the orthogonal-plane between θ=30° and 60° and θ=90° and 120° V-walls. Note that it has already been established from earlier experimental evidences that these two sets of V-walls lead to generally different flow behaviour. For θ=30° and 60° V-walls, the much earlier collisions of primary vortex-ring segments with the V-wall surfaces will lead to earlier initiation of circumferential flow along the vortex-ring filament and hence vortex compression along the orthogonal-plane. As such, this results in significant influx of compressed bi-helical lines around the primary vortex-ring cores towards the orthogonal-plane shortly after the collisions with the V-wall surfaces. Furthermore, the earlier collisions with the V-wall surfaces limit the extents

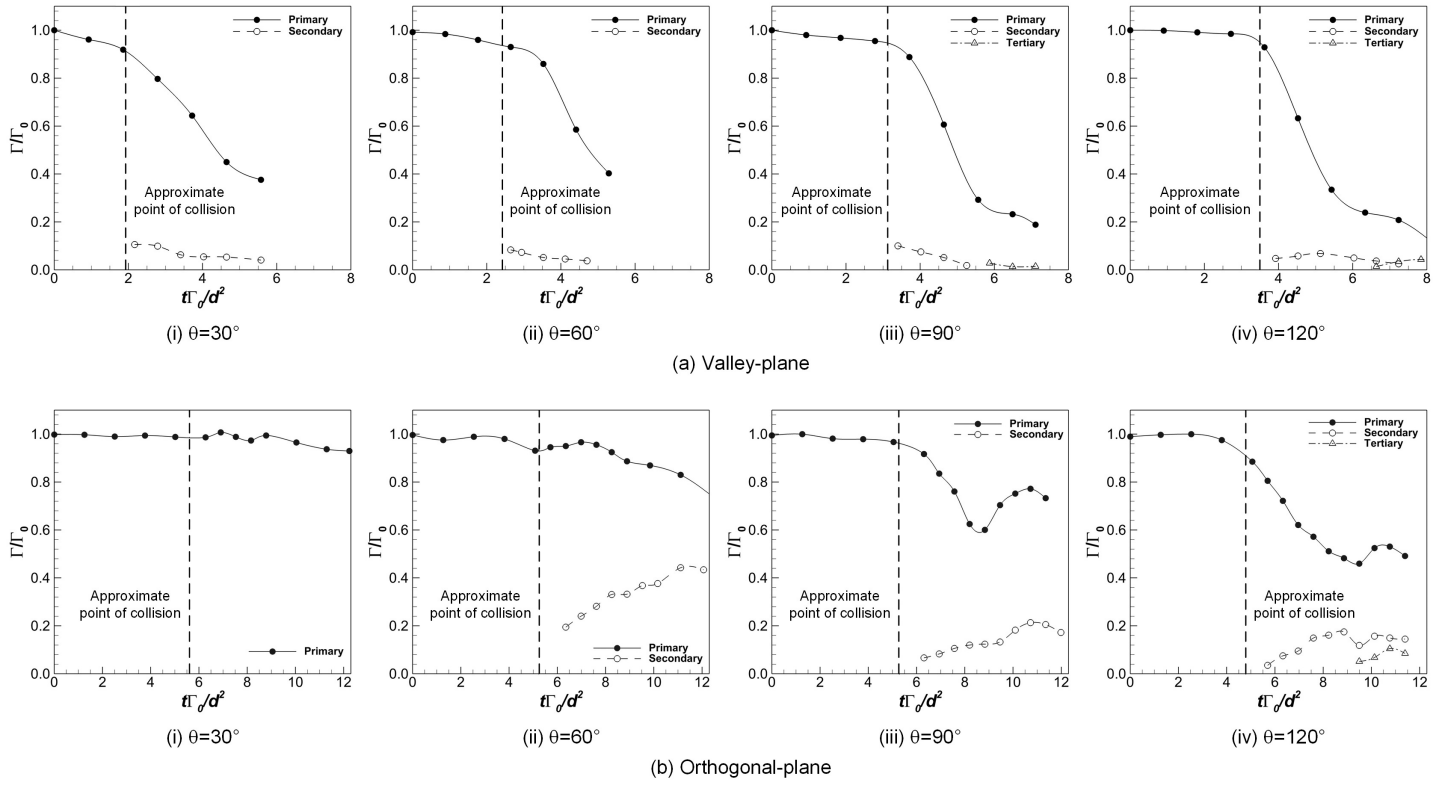

Figure 17: Changes to the primary, secondary and tertiary vortex-ring core circulation levels along the valley- and orthogonal-planes as the included-angle varies from θ=30° to 120°. Approximate points of collisions are indicated in the plots to better highlight when the primary vortex-ring collides with the V-walls. Note that the circulation levels are only determined when the vortex-cores are sufficiently discernible from the TR-PIV measurements.

to which the primary vortex-ring cores move away from the collision axis and hence vortex-stretching. These are likely to account for the much more gradual decreases in the overall primary vortex-ring circulations along the orthogonal-plane than those along the valley-plane. It has to be noted at this point, that due to the influx of compressed bi-helical lines occurring within close proximity of the primary vortex-ring cores, changes in the estimated circulation levels of the primary vortex-ring cores along the orthogonal-plane should be approached with care. The use of 2D TR-PIV measurement results here to estimate circulation levels means that it is not possible to distinguish between the local vorticities associated with the actual primary vortex-ring cores and compressed bi-helical lines. Hence, the overall primary vortex-ring core circulation should be treated as the total circulation arising from both vortical entities when vortex compression exists along the measurement plane, as opposed to the actual primary vortex-ring circulation.

As for θ=90° and 120° V-walls, they produce more gradual vortex compression along the orthogonal-plane due to smaller discrepancies between the times when the primary vortex-ring segments collide with the V-wall surfaces and the vertex of the valley. Additionally, their significantly larger included-angles allow the primary vortex-ring cores to move further away from the collision axis and hence, comparatively higher levels of vortex-stretching over the θ=30° and 60° V-walls. Based on Fig. 17(b)(iii) and 17(b)(iv), it is postulated that the vortex-stretching effects dominate over the more modest vortex compression effects, such that the overall primary vortex-ring circulations decrease for both θ=90° and 120° V-walls. This will agree well with the observation that the θ=120° V-wall producing a lower minimum overall primary vortex-ring core circulation level than the θ=90° V-wall, since the former will produce comparatively lower vortex compression and larger movements of the primary vortex-ring cores due to the larger included-angle. The small increments in the overall primary vortex-ring core circulations after they reached minimum levels may seem to run counter against Kelvin's theorem, where they should not increase due to preservation of circulation principle. However, as mentioned earlier, the estimated circulation levels here cannot differentiate contributions due to vorticities from the actual primary vortex-ring cores and compressed bi-helical lines. Hence, even as the primary vortex-ring cores cease to move away from the collision axis with reduced vortex-stretching levels due to significant interactions with the secondary and tertiary vortex-ring cores, continuing influx of compressed bi-helical lines towards the orthogonal-plane will eventually drive up the overall primary vortex-ring core circulation. Note the smaller extent to which the overall primary vortex-ring core circulation reaches its maximum level after the increment for the θ=120° V-wall as compared to θ=90° V-wall, which could be explained by lower vortex compression levels conferred by a larger included-angle V-wall. Last but not least, secondary vortex-ring core circulation levels for these two V-walls are significantly lower than their corresponding primary vortex-ring core counterparts and that of the θ=60° V-wall, with peak levels approximately half of that associated with the latter. Finally, tertiary vortex-ring core circulations estimated for this test case are lower than those of the secondary vortex-ring core circulations.

3.5. *Vortex-core trajectories and behaviour*

Since the V-walls used here are in principle geometrically similar to two symmetrically-arranged inclined-walls, it will be logical to compare the trajectories of the more dominant vortex-cores not only between the different V-walls here but also against those determined for inclined-wall studied earlier under similar experimental conditions [New *et al.* (2016)]. Note that the inclined surfaces associated with θ=120°, 60°, 30° V-walls here have the

same effective inclinations as the θ=30°, 60°, 75° inclined-walls studied earlier. Similar to New & Zang (2017), vortex-core locations were extracted from the flow visualization images based on image-processing procedures. It should be pointed out that comparisons of vortex-core trajectories are only conducted along the valley-plane, as the vortex-cores observed along the orthogonal-plane transit into flow incoherence too rapidly.

Comparisons of the vortex-core trajectories (not shown here for the sake of brevity) indicate that for the same primary vortex-ring Reynolds number and effective wall inclination, formations of secondary vortex-ring cores along the V-wall surfaces consistently initiate slightly earlier than those for inclined-walls. Since these results were obtained under the same conditions based on the same experimental setup (except for the walls used for vortex-ring collisions) as those in New *et al.* (2016), experimental inconsistencies are unlikely to be responsible for such consistent observation. Instead, it may be explained by the differences in the vortex-stretching/compression behaviour along the primary vortex-ring filament when it collides with a significantly less-constrained inclined-wall as opposed to a V-wall which is more physically constrained. For the former, the stretching of the vortex-ring segment that collides with the inclined-wall first will induce circumferential flows towards the vortex-ring segment that is diametrically opposite relatively unimpeded, where the latter continues to convect towards the wall. Even after the latter collides the wall, it can be observed from the flow visualization results in New *et al.* (2016) that it continues to convect further downstream along the inclined-wall surface without any physical constraints. This is particularly the case as the inclined-wall inclination becomes increasingly significant. In contrast, consider the same vortex-ring colliding with a V-wall of similar effective inclination, the vortex-stretching/compression behaviour will not play out so freely. In this case, there will actually be several vortex-segments undergoing stretching/compression behaviour simultaneously due to the two inclined-walls that make up each V-wall, as mentioned in the previous section when orthogonal-plane results were discussed.

To better explain this particular flow scenario and the resulting flow behaviour, Fig. 18 illustrates the flow dynamics as interpreted from the flow visualization results presented earlier. Note that the vortex-ring circumferential axis and vortex line nomenclature conform to those used by Lim (1989) for the sake of consistency. To begin, Fig. 18(a)(i) shows the primary vortex-ring translating towards the valley initially but remaining sufficiently far upstream such that the presence of the V-wall does not influence its behaviour. As it collides with the V-wall subsequently as shown in Fig. 18(a)(ii), vortex-ring segments impacting along the V-wall will decelerate and initiate the formation of the secondary vortex-ring, while the non-impacting vortex-ring segments along the orthogonal-plane continue to translate towards the valley bottom (see Fig. 18(b)(i)). Based on the earlier observations by Lim (1989) and New *et al.* (2016), the vortex line associated with the primary vortex-ring will take upon a bi-helical form around its circumferential axis and produces a circumferential flow from the vortex-ring segments that first collide with the inclined surfaces of the V-walls (i.e. valley-plane) towards the other segments that have not collided with any part of the V-wall (i.e. orthogonal-plane). In other words, earlier collisions between primary vortex-ring segments and the V-wall surfaces will produce a non-uniform secondary vortex-ring. Specifically, the secondary vortex-ring formation will initiate along the V-wall surfaces before propagating towards the orthogonal-plane gradually as other primary vortex-ring segments continue to translate towards the valley bottom, as depicted in Fig. 18(b)(i). The increasing proximity of the primary vortex-ring segments to the boundary layer closer to the valley bottom will gradually cause the latter to separate to form the rest of the secondary vortex-ring.

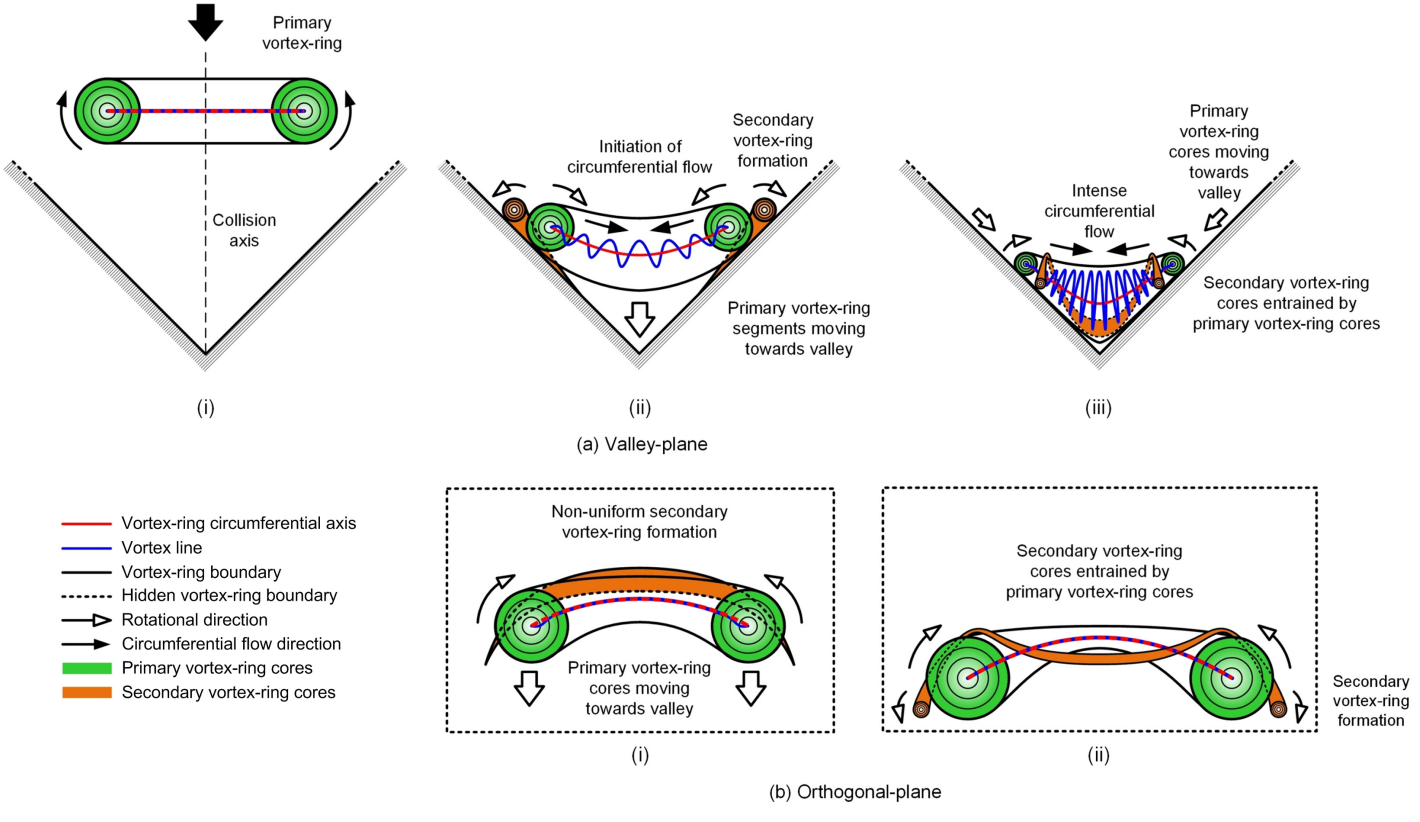

Figure 18: Flow dynamics along the (a) valley- and (b) orthogonal-plane as interpreted from the flow visualizations.

As the collision process continues, Fig. 18(a)(iii) shows the entrainment of the secondary vortex-ring cores by their primary vortex-ring counterparts along the valley-plane. Concurrently, the primary vortex-rings cores would have travelled further along both V-wall surfaces towards the valley bottom. This subsequently leads to comparatively more severe vortex compressions along the vortex-ring segments located along the orthogonal-plane, which will account for the rapid bulging and transition to incoherence in the primary vortex-ring cores observed earlier. It should however be noted that the heightened compression level would also limit the extent of circumferential flows and hence vortex-stretching behaviour along vortex-ring segments that had collided with the V-wall surfaces earlier on. This in turn suggests that higher adverse pressure gradients exist along the two inclined-surfaces of a V-wall, as compared to the scenario when only an inclined-wall is present. As a result, the wall boundary layers will separate earlier along the V-wall inclined-surfaces as compared to an equivalent inclined-wall, which would then support the vortex-core trajectory behaviour. On the other hand, formation of the secondary vortex-ring would have propagated till the orthogonal-plane as illustrated in Fig. 18(b)(ii). As the flow progresses, it is expected that increasingly more of the secondary vortex-ring will be entrained by the primary vortex-ring, after which the flow will become more incoherent due to the significant vortical interactions.

Finally, since New *et al.* (2016) and New & Zang (2017) had conducted vortex-ring collisions with other surface configurations using almost similar equipment and experimental conditions, it will be appropriate to take stock of the impact of surface configurations upon the primary vortex-ring behaviour, formation of secondary and tertiary vortex-rings and their mutual interactions after the collisions. Table 1 shows a brief summary of these behaviour associated with vortex-ring collisions with flat-wall, inclined-walls, round cylinders and the present V-walls. It is clear from the comparisons between the different flow configurations that outcomes from the vortex-ring collisions are highly sensitive towards the boundary conditions and it remains challenging to infer the outcome of one collision configuration based on another. Nevertheless, the availability of these observations arising from three systematic studies based on a common experimental setup and conditions will be useful to understand more complex collision scenarios in the future. It should also be noted that the different vortex-ring collision scenarios not only produce different vortex structures and behaviour, the timings at which these vortex structures formed after the collision will be of interest as well. This is particularly the case for asymmetric collision scenarios and when a systematic comparison of these timings has not been carried out previously. Since these timings are available from the two earlier and present studies, they were extracted from flow visualization video recordings captured at Re=2000 and 4000 and compiled here in Fig. 19. Note that only timings associated with collisions along the incline-plane of inclined-walls, convex-plane of round cylinders and valley-plane of V-walls will be of interest here, as they best reflect the impact of surface geometries upon vortex-ring collisions.

As the collisions of primary vortex-ring cores A and B (see Table 1) with the inclined-walls, as well as the resulting formations of their respective secondary vortex-ring cores, occur at different times, the time-intervals between their collisions and formation times (relative to A or B) were non-dimensionalized as before and shown in Fig. 19(a). The results portray a logical trend whereby the primary vortex-core collision time-interval ($\Delta\tau_p$) and secondary vortex-ring formation times (τ_s) become increasingly larger as the incline-angle increases, regardless of the exact Reynolds number. However, it is interesting to note that at Re=2000 here, the rate at which $\Delta\tau_p$ increases slows down while that of τ_s increases further as the incline-angle increases. As the Reynolds number doubled from Re=2000 to 4000, the collision time intervals and formation times decrease drastically.

Wall configuration	**Configuration and Reynolds number**	**Primary vortex-ring**	**Secondary-vortex-ring**	**Tertiary vortex-ring**
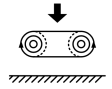 Flat-wall (New *et al.* (2016))	Re=2000	• Undergoes axisymmetric flattening, reduction in core diameter and increase in ring-diameter	• Fully entrained by primary vortex-ring	• Partially entrained by primary vortex-ring
	Re=4000	• Same as above but more rapid		• Fully entrained by primary vortex-ring
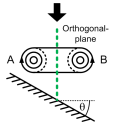 Inclined-wall ($\theta = 30°$, 45°, 60° and 75° incline) (New *et al.* (2016))	Re=2000 and 4000, incline-plane	• Vortex-core A rapidly reduces in core diameter upon collision • Vortex-core B becomes increasingly bulbous instead	• Fully entrained by vortex-core A and convects down inclined-wall • Partially entrained by vortex-core B except for $\theta = 30°$	• Fully entrained by vortex-core A • Not visibly formed at vortex-core B location
	Re=2000, orthogonal-plane	• Vortex cores undergo axisymmetric increase in vortex core diameter and ring-diameter	• Fully entrained by primary vortex cores	• Partially entrained by primary vortex ring cores at $\theta = 30°$ • Not visibly formed at $\theta = 60°$
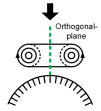 Round cylinder D/d=1, 2 and 4 (New & Zang (2017))	Re=4000, convex-plane	• Vortex-cores wrap around the convex surface and reduce in core diameter	• Formed at ϕ=31°, 57° and 92° for D/d=4, 2 and 1 cylinders • Fully entrained by primary vortex cores for D/d=4 • Partially entrained by primary vortex cores for D/d=1 and 2	• Partially entrained by primary vortex cores
	Re=4000, orthogonal-plane	• Undergoes axisymmetric flattening, reduction in core diameter and increase in ring-diameter	• Fully entrained by primary vortex-ring	• Partially entrained by primary vortex cores for D/d=2 and 4 • Fully entrained by primary vortex cores for D/d=1

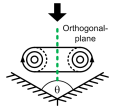 V-wall (θ=30°, 60°, 90° and 120°) (Present study)	Re=2000, valley-plane ($\theta = 90°$ and 120°)	• Vortex-cores undergo rapid reductions in core diameter • Significant movements down V-wall surface	• Fully entrained and merged with primary vortex-ring cores	Fully entrained by and merged with primary vortex-ring cores
	Re=2000, valley-plane ($\theta = 30°$ and 60°)	• Vortex-cores undergo rapid reductions in core diameter • Slight movements down V-wall surface	• Fully entrained and merged with primary vortex-ring cores • Leapfrog past primary vortex-ring cores for $\theta = 30°$	
	Re=4000, valley-plane ($\theta = 90°$ and 120°)	• Same as above but more rapid changes and significant movements down V-wall surface	• Fully entrained by primary vortex-ring cores • Leapfrog past primary vortex-ring cores for $\theta = 30°$	• Second set of tertiary vortices formed • Fully entrained by and merged with priamry vortex-ring core
	Re=4000, valley-plane ($\theta = 30°$ and 60°)		• Fully entrained and merged with primary vortex-ring cores	• Formation and entrainment of two sets of tertiary ring vortex- cores • Formation of multiple vortex-dipoles
	Re=2000, orthogonal-plane ($\theta = 90°$ and 120°)	• Vortex-cores undergo rapid increase in core diameter and flow incoherence as θ increases	• First formed along inner-edge and not entrained by primary vortex-ring cores	• One or more sets of tertiary ring vortex-cores formed and not entrained by primary vortex-ring cores
	Re=2000, orthogonal-plane ($\theta = 30°$ and 60°)		• First formed along V-wall surface and entrained by primary vortex-ring cores	• Not visibly formed

Table 1: Brief summary and comparisons between vortex-ring collisions upon flat-wall, inclined-walls, round cylinders and V-walls

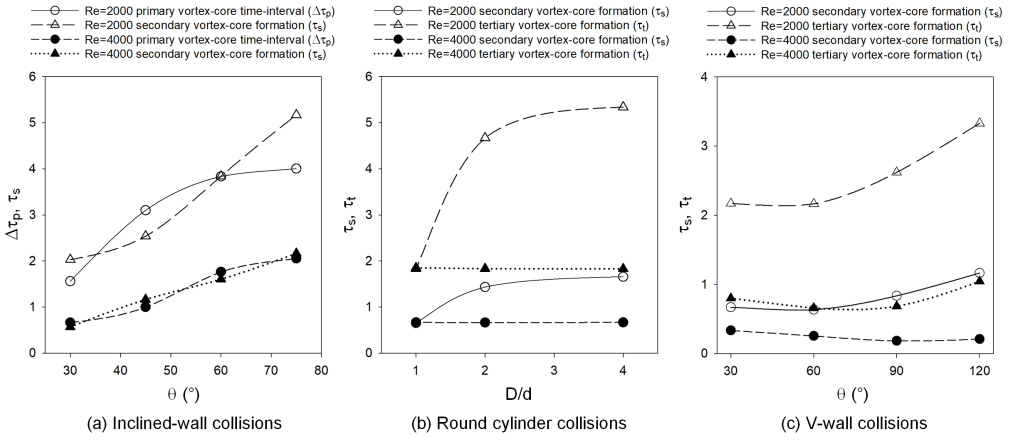

Figure 19: Comparisons of formation time-lags between diametrically opposite primary/secondary vortex-ring cores for (a) inclined-wall collisions, as well as formation times of secondary/tertiary vortex-ring cores for (b) round cylinder and (c) V-wall collisions. Empty symbols – Re=2000, filled symbols – Re=4000.

However, that should not come as a surprise as Table 1 has already provided indications that flow transitions will be more rapid at higher Reynolds numbers. Nevertheless, $\Delta\tau_p$ and τ_s increase in more linear-like manner at Re=4000 here. This also suggests that the collision times become less dependent on the exact Reynolds number and more directly upon the incline-angle, once a threshold Reynolds number is exceeded. The differences in the behaviour observed at the two different Reynolds numbers are likely due to the greater discrepancies in the non-linear vortex-stretching/compression behaviour for vortex-cores A and B.

Intriguingly, Fig. 19(b) shows that round cylinder based collisions demonstrate more consistent trends when it comes to secondary and tertiary vortex-ring core formation times (τ_t) at each Reynolds number used. For instance, τ_s and τ_t undergo significant increments before plateauing as the diameter-ratio increases from D/d=1 to 4 at Re=2000. Furthermore, τ_s and τ_t remain practically flat across all diameter-ratios at Re=4000. In contrast, inclined-wall and V-wall collisions produce less consistent trends at the same corresponding Reynolds numbers. In particular, note that flat-wall (i.e. assumed as $D/d \rightarrow \infty$) based collision leads to approximately τ_s=1.815 and τ_t=5.150 at Re=2000 and approximately τ_s=0.665 and τ_t=1.670 at Re=4000, which are close to the values observed for D/d=4 at the same Reynolds number (i.e. τ_s=1.660 and τ_t=5.340 at Re=2000, and τ_s=0.670 and τ_t=1.830 at Re=4000). Hence, this significantly strengthens the notion that round cylinder based collisions increasingly resemble that of flat-wall based collisions when the diameter-ratio increases [New & Zang (2017)]. Last but not least, V-wall based collision results are shown in Fig. 19(c), where τ_s and τ_t can be observed to increase with the included-angle. It should also be highlighted that the rate of increase grows as the included-angle increases, at least for Re=2000. In fact, note that τ_s=1.165 and τ_t=3.330 at Re=2000, and τ_s=0.210 and τ_t=1.045 at Re=4000, for θ=120° V-wall, which are approaching towards those for flat-wall (i.e. θ=180°) based collisions. Interestingly though, both τ_s and τ_t appear to decrease initially as the included-angle increases from θ=30° to 90°, before they increase at θ=120° for Re=4000.

Interestingly, round cylinder based collisions demonstrate more straight-forward correlations between the diameter-ratio and the secondary/tertiary vortex-ring core formation

times, followed by V-wall based collisions and then inclined-wall based collisions, at least for the range of physical configurations, vortex-ring conditions and Reynolds numbers used here. While this is surprising at the first instance since inclined-walls are physically closest to flat-walls, it may be better appreciated if one considers that inclined-wall collisions are asymmetrical while round cylinder and V-wall based collisions are not. For symmetrical surface geometries, the primary effects of the surface configuration (i.e. round or V-shaped) are expected to be in terms of vortex-stretching/compression effects conferred upon the various vortex-ring structures after the collisions, which occur symmetrically about the collision-axis in flat-wall, round cylinder and V-wall configurations. In contrast, vortex-rings colliding with inclined-walls are subjected to asymmetrical vortex-stretching/compression and secondary/tertiary vortex-ring formations, which would have led to highly asymmetrical and more complex three-dimensional mutual interactions between the primary, secondary and tertiary vortex-rings. As such, the correlation between the incline-angle and primary/secondary vortex-ring collision times could conceivably be weaker than those for round cylinder and V-wall based collisions.

4. Conclusion

Collisions between circular vortex-rings and V-walls were studied experimentally using LIF and TR-PIV techniques. Results show that while there exist some similarities between the present scenario and that associated with vortex-ring collisions upon flat inclined-walls, additional physical constraints imposed by the V-walls lead to more complex three-dimensional vortical changes. For instance, formations of secondary and tertiary vortex-ring segments along the orthogonal-plane lag behind those along the valley-plane (i.e. V-wall surfaces), since the primary vortex-ring collides with the latter earlier. Primary, secondary and tertiary-ring core sizes are observed to undergo significant reductions, that become progressively more rapidly as the included-angle reduces. Additionally, using a higher Reynolds vortex-ring and/or smaller included-angle will result in secondary and tertiary vortex-ring cores leapfrogging past the primary vortex-ring cores along the V-wall surfaces after their entrainment. This introduces adverse pressure gradients and produces wall-separated vortices upstream of the primary vortex-ring cores, the former of which pair up with the secondary and tertiary vortex-ring cores to form series of daisy-chained vortex-dipoles. Along the orthogonal-plane however, the primary vortex-ring cores become increasingly bulbous and incoherent as the flow progresses. Secondary vortex-ring cores are also observed along this plane at later times as well, when the secondary vortex-ring formation eventually propagates towards this plane. Interactions between the primary and secondary vortex-rings further give rise to additional vortex structures observed and movements of the former away from the collision-axis along this plane.

Circulations of the primary, secondary and tertiary vortex-ring cores determined from the TR-PIV measurements provide support for the notion that the flow behaviour for θ=30° to 60° V-walls differs from those associated with θ=90° to 120° V-walls. In particular, momentary increases in the primary vortex-ring core circulations along the orthogonal-plane are observed only for the latter configurations after they have been drastically reduced from the collisions. In addition, secondary vortex-ring core circulations tend to increase after they are formed along this plane, in contrast to the scenario along the valley-plane where they tend to decrease instead. Along the valley-plane, primary vortex-ring circulation decreases discernibly earlier for smaller included-angles, alongside with a more gradual reduction incurred after the V-wall

collisions. Vortex-core trajectory observations show slightly earlier secondary vortex-core formations in V-walls over inclined-walls of equivalent inclinations as well. The preceding observations can be accounted for by the bi-helical vortex line flow model proposed by Lim (1989) for vortex-ring collisions upon single inclined-walls. Unlike an inclined-wall however, V-walls possess two inclined-surfaces facing opposite towards each other about a symmetrical plane with a physically constrained valley where they meet at the vertex. As such, collision of each primary vortex-ring core upon each inclined-surface of every V-wall will cause the former vortex line to transit into bi-helical mode, thus driving circumferential flows from the collided vortex-ring segments along the valley-plane towards those along the orthogonal-plane. To illustrate this, a flow model is provided here to highlight the general behaviour of and interactions between primary and secondary vortex-rings after the collisions.

Last but not least, a comparison between vortex-ring collisions upon flat-walls, inclined-walls, round cylinders and the present V-walls conducted under similar experimental conditions by the authors previously is carried out to provide a more systematic overview on the range of collision behaviour and vortical outcomes. Furthermore, temporal information on the different primary vortex-ring core collision times, secondary and tertiary vortex-ring core formation times are extracted from the earlier and present studies to quantify the effects of Reynolds number, incline-angle, round cylinder diameter-ratio, and V-wall included-angle. The comparison shows that round cylinder and V-wall based collisions produce non-dimensionalized collision times that converge towards flat-wall based collisions more consistently when the diameter-ratio and included-angle become progressively larger, respectively. Interestingly, this appears to be less consistent for inclined-wall based collisions, presumably due to the asymmetrical formations of and interactions between various vortex-ring structures.

The authors acknowledge the support for the study by the School of Mechanical and Aerospace Engineering, Nanyang Technological University, Singapore, Singapore Ministry of Education AcRF Tier-2 grant (MOE2014-T2-1-002) and National Science Foundation of China grant (grant number: 11772197).

REFERENCES

Adhikari, D. & Lim, T. T. 2009 The impact of a vortex ring on a porous screen. *Fluid Dyn. Res.* **41** (5), 051404.

Amitay, M., Smith, D. R., Kibens, V., Parekh, D. E. & Glezer, A. 2001 Aerodynamic flow control over an unconventional airfoil using synthetic jet actuators. *AIAA journal* **39** (3), 361–370.

An, D., Warning, A., Yancey, K. G., Chang, C.-T., Kern, V. R., Datta, A. K., Steen, P. H., Luo, D. & Ma, M. 2016 Mass production of shaped particles through vortex ring freezing. *Nature Communications* **7**, 12401.

Arévalo, G., Hernández, R. H., Nicot, C. & Plaza, F. 2007 Vortex ring head-on collision with a heated vertical plate. *Phys. Fluids* **19** (8), 083603.

Cheng, M., Lou, J. & Lim, T. T. 2014 A numerical study of a vortex ring impacting a permeable wall. *Phys. Fluids* **26** (10), 103602.

Cheng, M., Lou, J. & Luo, L.-S. 2010 Numerical study of a vortex ring impacting a flat wall. *J. Fluid Mech.* **660**, 430–455.

Chu, C.-C., Wang, C.-T. & Chang, C.-C. 1995 A vortex ring impinging on a solid plane surface — vortex structure and surface force. *Phys. Fluids* **7** (6), 1391–1401.

Couch, L. D. & Krueger, P. S. 2011 Experimental investigation of vortex rings impinging on inclined surfaces. *Exp. Fluids* **51** (4), 1123–1138.

Didden, N. 1979 On the formation of vortex rings: rolling-up and production of circulation. *Zeitschrift für angew Mathematik und Physik* **30** (1), 101–116.

Fabris, D., Liepmann, D. & Marcus, D. 1996 Quantitative experimental and numerical investigation of a vortex ring impinging on a wall. *Phys. Fluids* **8** (10), 2640–2649.

Feng, H., Kaganovskiy, L. & Krasny, R. 2009 Azimuthal instability of a vortex ring computed by a vortex sheet panel method. *Fluid Dyn. Res.* **41** (5), 051405.

Gan, L., Dawson, J. R. & Nickels, T. B. 2012 On the drag of turbulent vortex rings. *J. Fluid Mech.* **709**, 85–105.

Gao, L. & Yu, S. C. M. 2010 A model for the pinch-off process of the leading vortex ring in a starting jet. *J. Fluid Mech.* **656**, 205–222.

Gharib, M., Rambod, E. & Shariff, K. 1998 A universal time scale for vortex ring formation. *J. Fluid Mech.* **360**, 121–140.

Gilarranz, J. L., Traub, L. W. & Rediniotis, O. K. 2005 A new class of synthetic jet actuators—part ii: application to flow separation control. *J. Fluid Engng* **127** (2), 377–387.

Glezer, A. 1988 The formation of vortex rings. *Phys. Fluids* **31** (12), 3532–3542.

Glezer, A. & Coles, D. 1990 An experimental study of a turbulent vortex ring. *J. Fluid Mech.* **211**, 243–283.

Goldstein, R. J. & Franchett, M. E. 1988 Heat transfer from a flat surface to an oblique impinging jet. *J. Heat Trans.* **110** (1), 84–90.

Hadžiabdić, M. & Hanjalić, K. 2008 Vortical structures and heat transfer in a round impinging jet. *J. Fluid Mech.* **596**, 221–260.

Hrynuk, J. T., Luipen, J. Van & Bohl, D. 2012 Flow visualization of a vortex ring interaction with porous surfaces. *Phys. Fluids* **24** (3), 037103.

Hu, J. & Peterson, S. D. 2018 Vortex ring impingement on a wall with a coaxial aperture. *Phys. Rev. Fluids* **3** (8), 084701.

Johnson, W. 2005 Model for vortex ring state influence on rotorcraft flight dynamics. *Tech. Rep.*.

Kaplanski, F., Sazhin, S. S., Fukumoto, Y., Steven, B. & Heikal, M. 2009 A generalized vortex ring model. *J. Fluid Mech.* **622**, 233–258.

Krueger, P. S., Dabiri, J. O. & Gharib, M. 2006 The formation number of vortex rings formed in uniform background co-flow. *J. Fluid Mech.* **556**, 147–166.

Krueger, P. S., Paul, S. & Gharib, M. 2003 The significance of vortex ring formation to the impulse and thrust of a starting jet. *Phys. Fluids* **15** (5), 1271–1281.

Leishman, J Gordon, Bhagwat, Mahendra J & Ananthan, Shreyas 2004 The vortex ring state as a spatially and temporally developing wake instability. *J. Am Helicopter Soc.* **49** (2), 160–175.

Lim, T. T. 1989 An experimental study of a vortex ring interacting with an inclined wall. *Exp. Fluids* **7** (7), 453–463.

Lim, T. T., Nickels, T. B. & Chong, M. S. 1991 A note on the cause of rebound in the head-on collision of a vortex ring with a wall. *Exp. Fluids* **12** (1-2), 41–48.

Mao, Xuerui & Hussain, F. 2017 Optimal transient growth on a vortex ring and its transition via cascade of ringlets. *J. Fluid Mech.* **832**, 269–286.

Mariani, R., Quinn, M. K., Kontis, K. & Marraffa, L. 2013 Shock-free compressible vortex rings impinging on a stationary surface: Effects of surface angle variation. *Exp. Therm Fluid Sci.* **47**, 126–142.

Martin, H. 1977 Heat and mass transfer between impinging gas jets and solid surfaces. *Adv. Heat Tran.* **13**, 1–60.

Maxworthy, T. 1972 The structure and stability of vortex rings. *J. Fluid Mech.* **51** (1), 15–32.

Minota, T., Nishida, M. & Lee, M. G. 1997 Shock formation by compressible vortex ring impinging on a wall. *Fluid Dyn. Res.* **21** (3), 139–157.

Mohseni, K. & Gharib, M. 1998 A model for universal time scale of vortex ring formation. *Phys. Fluids* **10** (10), 2436–2438.

Mohseni, K., Ran, H. & Colonius, T. 2001 Numerical experiments on vortex ring formation. *J. Fluid Mech.* **430**, 267–282.

Naaktgeboren, C., Krueger, P. S. & Lage, J. 2012 Interaction of a laminar vortex ring with a thin permeable screen. *J. Fluid Mech.* **707**, 260–286.

Naitoh, T., Banno, O. & Yamada, H. 2001 Longitudinal vortex structure in the flow field produced by a vortex ring impinging on a flat plate. *Fluid Dyn. Res.* **28** (1), 61.

Naitoh, T., Sun, B. & Yamada, H. 1995 A vortex ring travelling across a thin circular cylinder. *Fluid Dyn. Res.* **15** (1), 43.

New, T. H. & Long, J. 2015 Dynamics of laminar circular jet impingement upon convex cylinders. *Phys. Fluids* **27** (2), 024109.

New, T. H., Shi, Shengxian & Zang, B. 2016 Some observations on vortex-ring collisions upon inclined surfaces. *Exp. Fluids* **57** (6), 1–18.

New, T. H. & Zang, B. 2017 Head-on collisions of vortex rings upon round cylinders. *J. Fluid Mech.* **833**, 648–676.

New, T. H., Zang, B., Shi, Shengxian & Long, J. 2018 Impact of vortex-rings upon v-walls. In *In 19th International Symposium on the Application of Laser and Imaging Techniques to Fluid Mechanics*.

Newman, S., Brown, R., Perry, J., Lewis, S., Orchard, M. & Modha, A. 2001 Comparative numerical and experimental investigations of the vortex ring phenomenon in rotorcraft. In *57th Annual Forum of American Helicopter Society*.

Nitsche, M. & Krasny, R. 1994 A numerical study of vortex ring formation at the edge of a circular tube. *J. Fluid Mech.* **276**, 139–161.

Orlandi, P. 1993 Vortex dipoles impinging on circular cylinders. *Phys. Fluids A* **5** (9), 2196–2206.

Orlandi, P. & Verzicco, R. 1993 Vortex rings impinging on walls: axisymmetric and three-dimensional simulations. *J. Fluid Mech.* **256**, 615–646.

Ponitz, B., Sastuba, M. & Brücker, C. 2016 4d visualization study of a vortex ring life cycle using modal analyses. *J. Visual.* **19** (2), 237–259.

Pullin, D. I. 1979 Vortex ring formation at tube and orifice openings. *The Phys. Fluids* **22** (3), 401–403.

R. S. Heeg, RS & Riley, N. 1997 Simulations of the formation of an axisymmetric vortex ring. *J. Fluid Mech.* **339**, 199–211.

Ren, H., Zhang, G. & Guan, H. 2015 Three-dimensional numerical simulation of a vortex ring impinging on a circular cylinder. *Fluid Dyn. Res.* **47** (2), 025507.

Shusser, M., Rosenfeld, M., Dabiri, J. O. & Gharib, M. 2006 Effect of time-dependent piston velocity program on vortex ring formation in a piston/cylinder arrangement. *Phys. Fluids* **18** (3), 033601.

Swearingen, J. D., Crouch, J. D. & Handler, R. A. 1995 Dynamics and stability of a vortex ring impacting a solid boundary. *J. Fluid Mech.* **297**, 1–28.

Verzicco, R. & Orlandi, P. 1994 Normal and oblique collisions of a vortex ring with a wall. *Meccanica* **29** (4), 383–391.

Walker, J. D. A., Smith, C. R., Cerra, A. W. & Doligalski, T. L. 1987 The impact of a vortex ring on a wall. *J. Fluid Mech.* **181**, 99–140.

Weigand, A. & Gharib, M. 1997 On the evolution of laminar vortex rings. *Exp. Fluids* **22**, 447–457.

Xu, Y. & Wang, J.-J. 2016 Flow structure evolution for laminar vortex rings impinging onto a fixed solid wall. *Exp. Therm. and Fluid Sc.* **75**, 211–219.

Xu, Y., Wang, J.-J., Feng, L.-H., He, G.-S. & Wang, Z.-Y. 2018 Laminar vortex rings impinging onto porous walls with a constant porosity. *J. Fluid Mech.* **837**, 729–764.

You, D. & Moin, P. 2008 Active control of flow separation over an airfoil using synthetic jets. *J. Fluids Struc.* **24** (8), 1349–1357.

Zhan, Y., Yan, N., Li, Y., Meng, Y., Wang, J., Zhang, N., Yu, Q. & Xia, H. 2017 Fabrication of graphene millimeter-vortex ring with excellent absorption via solution dripping and in-situ reduction method. *Chem. Engng J.* **327**, 142–149.